FINITE ELEMENT MODELING OF ARC WELDED JOINT BASED ON THE EXPERIMENTAL STUDIES OF THE WELDMENT

By
Tamrin Tanha

A Thesis Submitted to the Faculty of Graduate Studies of

The University of Manitoba

In partial fulfilment of the requirements of the degree of

MASTER OF SCIENCE

Department of Mechanical Engineering

University of Manitoba

Winnipeg, Manitoba

ABSTRACT

The structural integrity of a welded structure depends mainly on the performance of the welded joints. Due to the welding process, the mechanical properties of the structure change and different regions are created in the weldment. The mechanical properties of welded joints change significantly around the heat affected zone (HAZ). So to predict stress distribution around the weld, these changes should be considered in the finite element model (FEM) of the welded structure. In this research, the changes of mechanical properties around the welded joint were experimentally tested and used to develop a FEM model of a welded joint which can predict the stress behavior around the weld. First, an experimental analysis was carried out on an ASTM standard arc welded joint of stainless steel specimen to observe the microstructural change in the HAZ. This enables to find out the HAZ width using an optical microscope. Moreover, a tensile testing was performed to investigate the change of Young's modulus of the HAZ compared to the base metal (BM). Another experimental analysis was also performed on a real arc welded structure of the same material to observe its' strain distribution around the HAZ. The HAZ width and Young's modulus obtained from the experimental testing were then applied to generate the FEM model of an ASTM standard arc welded joint as well as a real arc welded structure of stainless steel. The finite element analysis (FEA) results of stress distribution around the weld joint in both cases show a good agreement with the experimental results. Therefore, the developed material property based FEM model can predict the stress behavior of similar type of structures with the same welding process on the same material studied in this research.

ACKNOWLEDGEMENTS

I would like to express my sincere gratitude to my advisor, Dr. Christine Q. Wu and Dr. Nan Wu for their full support, expert guidance, encouragement and assistance throughout this work. I am thankful for their valuable time, patience, counsel and insight to carry out this thesis. This thesis would not have been possible without their supervision and care.

Along with my advisors, I would like to thank Dr. Olanrewaju Ojo for his help in testing of the specimens. He and his student Asala Gbenga were very helpful to guide me while performing the test in their lab.

I am also grateful to Mr. Daniel Godin from Industrial Technology Center (ITC) for his assistance and technical support in this research. I would like to thank my colleague Md. Nuruzzaman and Khashayar Pejhan for their help in this research. I would like to give a special thanks to Anton Kuznetcov for his help and guidance in finite element analysis work. I am also thankful to my friends Rony C. Shaha and Ebadur Rahman for their continuous support.

Last but not the least I want to thank my parents, my younger brother Upal and my husband Tareq for their enormous help and motivation. Specially, I would like to thank my mother for her inspiration without which it is not possible for me to achieve my goals.

DEDICATION

I would like to dedicate this thesis to my parents for the sacrifices they made for me and for always believing in me.

TABLE OF CONTENTS

ABSTRACT ii

ACKNOWLEDGEMENTS iii

DEDICATION iv

TABLE OF CONTENTS v

LIST OF FIGURES ix

LIST OF TABLES xii

LIST OF SYMBOLS xiii

1. INTRODUCTION 1

1.1 Motivation of this Research 1

1.2 Objective 2

1.3 Outline of the Thesis 4

2. LITERATURE REVIEW 6

2.1 Welding 6

2.1.1 Welding Techniques 7

2.1.2 Welding Design 8

2.2 Mechanical Property Change in weldment and Significant Factors that affect the Mechanical Property Change 9

2.3 Finite Element Modeling of Welded Joint 17

3. METHODOLOGY 24

3.1 Workflow Outline 24

3.2 Experimental Analysis 26

3.2.1 ASTM Standard Specimen 26

3.2.1.1. Microscopic Observation and Measurement of HAZ width:........................ 26

3.2.1.2 Tensile Test 31

3.2.2 Window Pillar Structure 37

3.2.2.1 Testing under Braking Load 37

3.2.2.2 Tensile Testing of the Base Material Sample 40

3.3 Finite Element Modeling based on Experiment.. 40

3.3.1 ASTM Standard Specimen 40

3.3.1.1 Geometry.. 40

3.3.1.2 Meshing.. 41

3.3.1.3 Boundary conditions 43

3.3.1.4 Material Properties.. 43

3.3.1.5 Simulation 44

3.3.2 Window Pillar Joint 44

3.3.2.1 Geometry.. 45

3.3.2.2 Meshing.. 46

3.3.2.3 Connections.. 49

3.3.2.4 Boundary Conditions 51

3.3.2.5 Material Properties of Full Model 52

3.3.2.6 Initial Simulation 52

3.3.2.7 Cut boundary Interpolation 53

3.3.2.8 Verification of Submodel 53

3.3.2.9 Material property of Submodel 56

3.3.2.10 Final Simulation 56

4. RESULTS AND DISCUSSION 57

4.1 Experimental Results 57

4.1.1 Determination of Heat Affected Zone Width of ASTM standard Specimen 57

4.1.2 Determination of Material Properties of Heat Affected Zone (HAZ) and Base Metal (BM) Zone of ASTM Standard Specimen 59

4.1.3 Braking Load Testing of Window Pillar Structure 61

4.1.4 Determination of Material Properties of Base Metal of Window Pillar Structure 62

4.2 Finite Element Analysis (FEA) Result 62

4.2.1 ASTM Standard Specimen 62

4.2.2 Window Pillar Structure 65

4.2.3 Comparison of Material Based Model and Effective Notch Model 70

5. CONCLUSIONS AND FUTURE WORK 75

6. REFERENCES 78

APPENDIX A- STRAIN DATA OF ASTM STANDARD SPECIMEN................................ 84

LIST OF FIGURES

Figure 1: Interaction between heat source and base metal in weldment [6] 6

Figure 2: Types of Welded Joint – (a) Square butt joint, (b) V butt joint, (c) Lap joint, (d) T-joint [2] 8

Figure 3: Three (3) distinct zones in the weldment 9

Figure 4: Yield stress and strain value comparison for base metal and different welding types studied by Yayla et al. [13] 12

Figure 5: Hardness variation across base metal, HAZ and weld metal regions [13] 13

Figure 6: UTS, YS and strain hardening distribution [14] 14

Figure 7: Young's Modulus Variation across the weld zone [18] 16

Figure 8: Poisson's ratio variation across the weld zone [18] 16

Figure 9: Work Flow Outline of the Research 25

Figure 10: ASTM Standard Arc Welded Specimen 26

Figure 11: Sectioned ASTM Standard Sample 28

Figure 12: Machine used for Grinding 29

Figure 13: Polishing Machine 29

Figure 14 : Prepared Sample for Microscopic Observation 30

Figure 15: Optical Microscope used for Microscopic Observation 31

Figure 16: Typical Curve for a Material Subjected to Tensile Load [41] 32

Figure 17: Strain Rosette for Strain Measurement 33

Figure 18: a) MTS Tensile Testing Machine (30 KN) b) 32-channel data acquisition system (DAQ) 35

Figure 19: Tensile Testing Setup 36

Figure 20: Strain Gauge Location on ASTM Standard Specimen 36
Figure 21: Window Pillar Structure of a Multi Passenger Bur Structure 37
Figure 22: Braking Load Condition of the Window Pillar Structure 38
Figure 23: Strain Gauge Location a) at Front Side b) at Back Side 39
Figure 24: Finite Element Model of ASTM Standard Specimen 41
Figure 25: Meshing of finite element model of ASTM standard specimen 42
Figure 26: Mesh Convergence Study of FE Model of ASTM Standard Specimen 42
Figure 27: Boundary Conditions of FE Model of ASTM Standard Specimen 43
Figure 28: Initial Full Model of Window Pillar Structure 45
Figure 29: Submodel Geometry a) Front b) Back and c) Heat Affected Zone (HAZ) Location .. 46
Figure 30: Meshing of a) Full Model b) Submodel c) Critical Region of Submodel 47
Figure 31: Mesh Convergence Study of Full Model of Window Pillar 48
Figure 32: Mesh Convergence Study of Submodel of Window Pillar 48
Figure 33: Bonded Contacts of Full Model 49
Figure 34: Frictional Contacts of Full Model 50
Figure 35: Contact Regions of the Submodel a) Bonded Contact b) Frictional Contact 51
Figure 36: Boundary Conditions of the Full Model 52
Figure 37: Cut Boundary Interpolation from Full Model to Submodel 53
Figure 38: Equivalent Stress Distribution a) Full Model b) Submodel 54
Figure 39: Equivalent Stress Distribution at Cut Boundary a) Full Model b) Submodel 55
Figure 40: Microstructural Difference between Base Metal, Heat Affected zone and Fusion Zone 58
Figure 41: Heat Affected Zone Width 59

Figure 42: Normal Strain Distribution at Strain Gauge 1 Position 59
Figure 43: Strain Gauge 1 Attached at Heat Affected Zone 60
Figure 44: Stress vs. Strain Curve for a) Heat Affected Zone b) Base Metal Zone 61
Figure 45: Heat Affected Zone width in Finite Element Model of ASTM Standard Specimen .. 63
Figure 46: Normal Strain Distribution in the Loading Direction of ASTM Standard Specimen in FEA a) Top b) Bottom 63
Figure 47: Comparison of Normal Strain Distribution between Experimental and FEA Result at Strain Gauge 1 Location 64
Figure 48: Front Submodel a) Equivalent Stress Distribution b) Strain Gauge Location 66
Figure 49: Back Submodel a) Equivalent Stress Distribution b) Strain Gauge Location............. 67
Figure 50: Direction of Heat Affected Zone Width Increase 68
Figure 51: FEA Stress Behavior of the Window Pillar Structure 70
Figure 52: Comparison between Material Based Model and Effective Notch Model Stress at Strain Gauge 1, 2 & 5 Location 72
Figure 53: Comparison between Material Based Model and Effective Notch Model Stress at Strain Gauge 3, 4 & 6 Location 72

LIST OF TABLES

Table 1: Comparison of Equivalent Stress... 55

Table 2: Mechanical Properties used in ASTM standard FE Model 63

Table 3: Comparison of Experimental and FEA result at Strain Gauge 1 Location of ASTM standard Specimen 64

Table 4: Mechanical Properties used in Window Pillar FEM Model... 65

Table 5: Equivalent Stress Distribution at Strain Gauge 1, 2 & 5 Location of FEM Model Window Pillar Structure 66

Table 6: Equivalent Stress Distribution at Strain Gauge 3,4 & 6 Location of FEM Model Window Pillar Structure 67

Table 7: Normal and Shear Strain Data at Strain Gauge 1 (Heat Affected Zone) Location......... 84

Table 8: Normal and Shear Strain Data at Strain Gauge 2 (Base Metal) Location 84

LIST OF SYMBOLS

ASTM	American Society for Testing and Materials
HAZ	Heat Affected Zone
BM	Base Metal
WM	Weld Metal
FZ	Fusion Zone
FEM	Finite Element Method
FEA	Finite Element Analysis
FE	Finite Element
E	Young`s Modulus
ν	Poisson Ratio
ε_x	Normal Strain in X-direction
ε_y	Normal Strain in Y-direction
Υ_{xy}	Shear Strain
ε_1	Maximum Principle Strain
ε_2	Minimum Principle Strain
Υ_{12}	Maximum Shear Strain
σ_1	Maximum Principle Stress
σ_2	Minimum Principle Stress
σ_{vm}	Equivalent Stress

CHAPTER 1

INTRODUCTION

1.1 Motivation of this Research

Structural integrity is a very important term for any engineering structure. Safety, longevity and functionality of any structure specially ground vehicles greatly depend on the structural integrity. Structural integrity generally refers as the ability to endure a designed load of a structure and to resist failure. Ground vehicle manufacturers always desire for a reliable and long-running structure that will last for many years. The idea of structural integrity is used to design a structure that will perform satisfactorily under a design load for the desired service life [1]. It is very much important to accurately assess the structural behavior before launching any product.

Nowadays, most of the vehicle structure consists of a number of welds. The integrity of welded vehicle structure depends on the performance of the welded joints. The structural integrity of an engineering structure depends on the different mechanical properties of the material such as roughness, toughness, hardness, elasticity etc. [1]. Due to the welding process, these mechanical properties of the structure change significantly and different regions are created in the weldment. The mechanical property changes in the HAZ adjacent to weld are very significant [2]. These changes considerably affect the behavior of the structure. It is extremely important to consider these material properties change during the design process of any welded vehicle structure [3].

Many ground vehicle structures experience fracture or crack near or around the welded joint after a cycle of running. It mainly happens because the required details of welding phenomenon were not considered during the design process. This results in failure at an unexpected region which was not critically considered during the preliminary design. This failure shortens the lifetime of a structure. Due this unexpected fracture or failure, sometimes vehicle structures needed to repair or renovate. These associates with unexpected renovation and labor cost etc. Thus, vehicle companies face a major economic loss. This type of failure can be catastrophic also.

In order to solve this problem, it is required to consider welding details and resulting mechanical property changes within the structure due to welding. It will help to obtain reliable stress distribution of the whole structure as well as around the welds.

Finite element method (FEM) is widely used to model and simulate the vehicle structural behavior. Its efficient uses ensure proper stress distribution of a structure. Nowadays, it is one of the widely used tools for stress analysis of a structure.

It is a unique challenge to develop a proper FEM model of welding which can analyze both stress distribution and find out critical areas of a structure. The material property changes due to welding should be incorporated in the model to develop a proper FEM model of a weld. There are different methodologies on which researchers are working to prepare a welding model which is reliable, convenient for the designers and easy to simulate.

1.2 Objective

This work is mainly focused on developing a FEM model of arc welded window pillar joint of a real multi-passenger bus structure based on experimental testing results. The main objective of this work is to prepare a FEM model of a welded joint which can predict stress behavior and critical location of a ground vehicle structure. The FEM model is generated based on the size and the Young's modulus heat affect zone (HAZ) obtained from experimental studies. Two welded specimens are used, one is ASTM standard arc welded sample and another is an arc welded window pillar arc welded joint of a real multi-passenger bus structure. Both of these samples are made of stainless steel with the same type of welded joint (Butt Weld). They are manufactured under same welding condition. This research is focused on the stainless steel arc welded joint as this material is widely used in different engineering structure.

To comply with the main objective of this thesis, the work is broken down into the following sections:

a) Find out the width of HAZ adjacent to weld of ASTM standard specimen using an optical microscope;
b) Perform tensile testing of an ASTM standard specimen to find out the Young's modulus of HAZ and BM from the stress vs. strain curve and also the Poisson ratio of HAZ and BM;
c) Validate the FEM model of ASTM standard specimen using the obtained Young's modulus;
d) Carry out the testing of window pillar joint of a real bus structure under braking load which is one important loading condition and collect strain data from some critical point;
e) Perform tensile testing of BM sample of window pillar joint to find out the Young's modulus from stress vs. strain curve;
f) Create a FEM model of the window pillar joint using the mechanical properties of HAZ derived from the ASTM standard specimen and mechanical properties of BM obtained from the tensile testing of BM sample of the window pillar;
g) Validate the FEM model of window pillar joint by comparing the numerical results with the experimentally obtained result under braking load condition;

1.3 Outline of the Thesis

In Chapter 2, the literature review of welding and its different finite element modeling procedures are discussed. In the first part of literature review, Section 2.1, the basic welding process and different area of application of welding are presented. In Section 2.2, material property changes in the weldment and important factors that significantly affect these properties are summarized based on the previous research work. Moreover, the different zone in the weldment i.e. BM zone, FZ and HAZ and their change in mechanical property due to welding are elaborately discussed in these sections. The discussions related to different types and techniques of finite element modeling of welded joint experimented by the researchers are presented in Section 2.3.

In Chapter 3, the details methodology of this work is discussed with all necessary details. Section 3.1 presented a brief overview of the full research work. In Section 3.2, the experimental procedure of finding the HAZ width and mechanical properties of HAZ and BM zone of ASTM standard specimen are discussed. This section also presents the experimental procedure to find out the strain at different critical location of window pillar structure under braking load. The finite element modeling procedure of ASTM standard specimen and window pillar joint are elaborately demonstrated in Section 3.3.

The experimental and numerical results and necessary discussions are presented in Chapter 4. In section 4.1, the experimental analysis results of ASTM standard specimen and window pillar joint are discussed. In this section, the obtained HAZ width and mechanical properties of HAZ and BM zone of ASTM standard specimen are described along with the strain value results of window pillar joint under braking load at different critical locations. This section also presents the mechanical properties of BM of window pillar structure.

The finite element analysis (FEA) results are presented in Section 4.2. In this section, FEA of ASTM standard specimen and window pillar joint are described. The detail validation procedure of FEM models i.e. comparison between experimental and numerical result are described in this section also.

Conclusions and the future works are described in Chapter 5. References and appendix are added afterward.

CHAPTER 2

LITERATURE REVIEW

2.1 Welding

Now a days, different types of material joining process are used to joint two similar or dissimilar metals. Adhesive bonding, soldering, brazing, welding etc. are some common method to join materials. Each of these processes has their own application. The selection of particular process depends on design requirements, automation and design assembly. Among all these processes, welding is one of the most useful and popular metal joining process. This process is now widely used. It is also considered as one of the cost effective process [4].

In welding process, two metals or thermoplastic are joined together by the application of heat. It has a difference from brazing and soldering process because in this process BM melts. A filler metal is often required also to form a weld pool which eventually cools to form a strong joint like base material. Sometimes pressure is also used to produce weld in conjunction with heat or by itself [5].

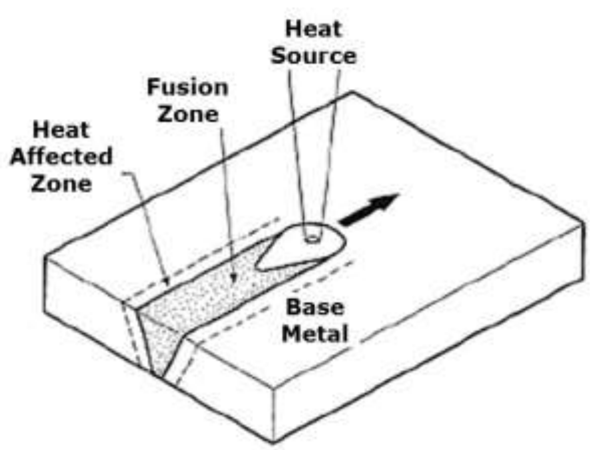

Figure 1: Interaction between heat source and base metal in weldment [6]

2.1.1 Welding Techniques

Selection of appropriate welding process for a specific application is one the important issue. There are several types welding techniques available. These different types of welding are generally used in automobile industry, structural works, machine repair works, refineries and fabrication of pipe line. Some of the well-known welding methods are shielded metal arc welding (SMAW), gas tungsten arc welding (GTAW), gas metal arc welding (GMAW), submerged arc welding (SAW), flux-cored arc welding (FCAW), electro-slag welding etc. These different welding processes are carried out with different types of energy source under different environment [5].

Among the above mentioned welding process, the gas metal arc welding (GMAW) process is one of the prominent metal joining process which is used worldwide. This process is also termed as metal inert gas (MIG) welding and it is less commonly known as metal active gas (MAG) welding process. In this process, metal joints are produced by the heating effect of a continuously fed filler metal electrode and the work. In order to protect the molten weld pool, this process requires shielding from an externally supplied gas [7].

In present day’s, gas metal arc welding (GMAW) enjoys worldwide popularity because of its ability to produce weld of desired quality for wide range of ferrous and non-ferrous alloy and cost-effectiveness [7]. The other advantages of this process are as follows:

a) This process is useful for wide range of material type and thickness which gives manufacturers much flexibility.
b) This has higher electrode efficiency compared to other process.

c) This process is capable for all welding position.

d) Weld bead appearance is very good

e) Minimum amount of weld spatter and slag makes weld clean up quick and easy.

f) This welding process requires lower heat input compare to other process.

These advantages make gas metal arc welding (GMAW) process as one the most popular welding process in the industrial application.

2.1.2 Welding Design

Welding joint design is another important factor. Geometrically a welded joint can be produced in different ways depending on the particular requirement. Some welding is suitable only for some specific design. The type of welded joint geometry can be categorized into five ways: butt joint, lap joint, corner joint, edge joint, and T-joint. Again butt joint can be square type, single V type and double V type [5].

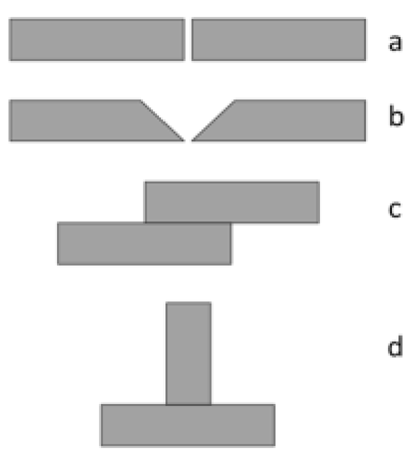

Figure 2: Types of Welded Joint – (a) Square butt joint, (b) V butt joint, (c) Lap joint, (d) T-joint [2]

Welding is a common process that is used in any industry. For suitable and efficient application of welding process it is necessary to determine appropriate welding process for a specific joint.

2.2 Mechanical Property Change in weldment and Significant Factors that affect the Mechanical Property Change

During the welding process, the interactions of heat source with the material results sever thermal change. These thermal excursions experienced by the weldment vary from region to region. As a result, three distinct zones are created in the weldment. These three (3) zones are unaffected parent metal or BM zone, weld metal (WM) or fusion zone (FZ) and HAZ [6].

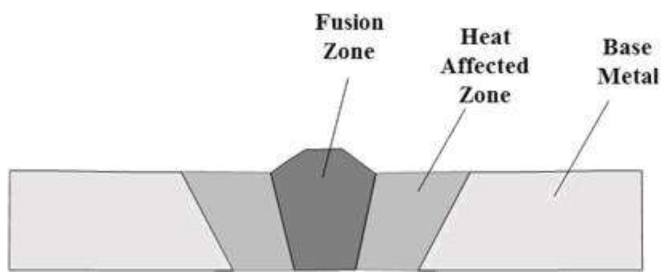

Figure 3: Three (3) distinct zones in the weldment

The FZ and HAZ experience changes in microstructure and mechanical properties. These changes generally effected by the melting and solidification behavior of weld pool [6].

The HAZ is a part of BM which is either metal or thermoplastic. This area is not meted but its mechanical and microstructural property significantly changes due to the heat intensive cutting operation during welding. The generated heat from the welding and following re-cooling process generates this change from the fusion line or weld interface to the end of sensitizing temperature in the BM. The extent of this change depends primarily on the filler metal, BM and heat input during the welding process. There are also many other factors which effects these changes [8].

The phase transformations, dissolution of strengthening precipitates and re-precipitation of particles during a post-weld heat treatment are some effect of the thermal cycle. Due to these effects, several sub-regions are observed in the HAZ in terms of different microstructure and properties. These depends the actual thermal history of each region [9].

Many researchers had worked on different type of welded joint of different welding process to study the change of these mechanical properties and microstructure of welded joint. Research has been ongoing to investigate the mechanical behavior change in the weldment and to identify significant factor which causes these changes. Some research are extensively based on the analysis of microstructural and hardness change in the weldment while some mainly focused on the different mechanical property change i.e. change in tensile yield strength, Young's modulus and Poisson ratio.

In 1991 Joarder *et al.* conducted a study to investigate the microstructure of single passed submerged arc welded (SAW) joint of 1.2 cm thick carbon steel plate. For this purpose, two types of microscope i.e. optical microscope and transmission electron microscope (TEM) were used. Under the optical microscope clearly distinct microstructure of BM, HAZ and WM zone were observed. After that, transmission electron microscope (TEM) was used to study the finer details of HAZ and WM zone. From these study three different sub zones of HAZ was observed i.e. spheroidzed, partially transformed, grain-refined and grain coarsened. The top, middle and base of the weld metal also exhibit different microstructure [10]. A number of studies were also performed later to observe the microstructural change of different types of weld of different material.

Missori *et al.* performed an investigation on the microstructure and mechanical characteristics change in gas metal arc welded (GMAW) joint (four passes) of 6082-T6 aluminum alloy plates in 2000. They performed some experimental work on Vickers micro-hardness test, tensile test, fatigue rotating bending test, impact test and scanning electron microscopy. In this experiment 10 mm thick plate of 6082-T6 aluminum alloy were used. The specimen gauge length was 80 mm and 20x10 mm2 rectangular sections [11].

In this study a remarkable reduction in the tensile strength of the welded 6082-T6 aluminum joint was found compared to the base material. Both the tensile strength and hardness in the HAZ were reduced to minimum at 6 mm distance from the fusion line. One of the important finding was that fracture occurred in the HAZ of the specimen in tensile test while for fatigue test the fracture location is WM zone. It is also noticeable that fatigue failure occurred earlier in welded specimen compared to the unwelded one [11].

Beghini *et al.* performed an analysis to evaluate the mechanical properties of welded joints of small specimen in 2001. Here some small tensile test specimens were collected from a large pipe structure. In this study, three (3) small tensile test specimens were collected from each zone of the weldment (BM, WM and HAZ). The cross sectional area was nearly 1 mm^2 (thickness -0.7 mm and width 1.5mm) All these joints are double V but welded joint [12]. Submerged arc welding (SAW) process was used to produce these joint. In this experiment yield strength of BM, WM and HAZ were compared. The term mismatch was used for comparison purpose. The difference between the two results is termed as mismatch. For example, if WM exhibits lower strength than BM then it is called under-matched condition but it the strength of WM is higher, then it will be over-matched condition. The results showed WM zone and HAZ overmatch the base material. For the weld metal overmatch was high and which was about 20% [12].

In literature, some studies were also done to find out the effect of different welding process on the structure. Yayla *et al.* studied with different welding technique to evaluate the mechanical properties of steel weldment in 2006. In this experiment, shielded metal arc welded (SMAW), gas metal arc welded (GMAW) and submerged arc welded (SAW) HY-80 steel specimen were used. The objective of this study was to find out the optimum welding technique for steel. For this purpose, they have done some tensile testing, impact testing of these joints. Hardness profiles of the weldment were also observed. The dimension of tensile testing specimen and hardness measurement specimen was 5 x 12.5 mm and 10 x 20 x 80 mm respectively.

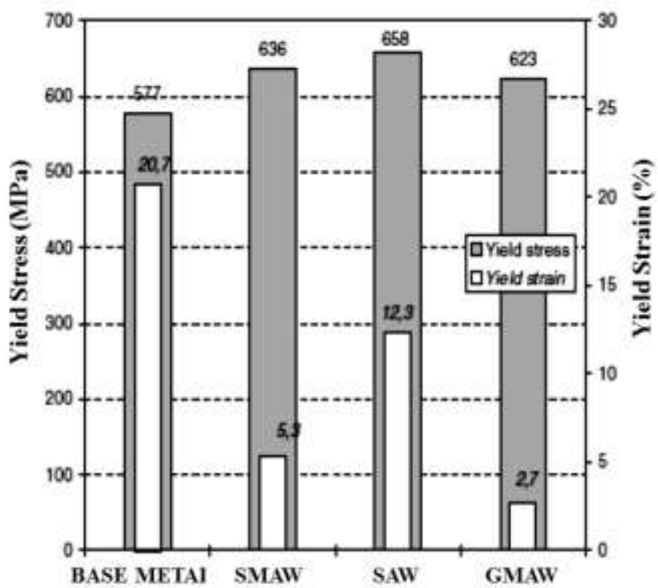

Figure 4: Yield stress and strain value comparison for base metal and different welding types studied by Yayla et al. [13]

Important outcome of this test was that the fracture occurred at the base material. The strength of both HAZ and WM zone was not lower than the BM [13]

The hardness profile was also different for WM and HAZ region. The highest hardness value was obtained is HAZ region [13].

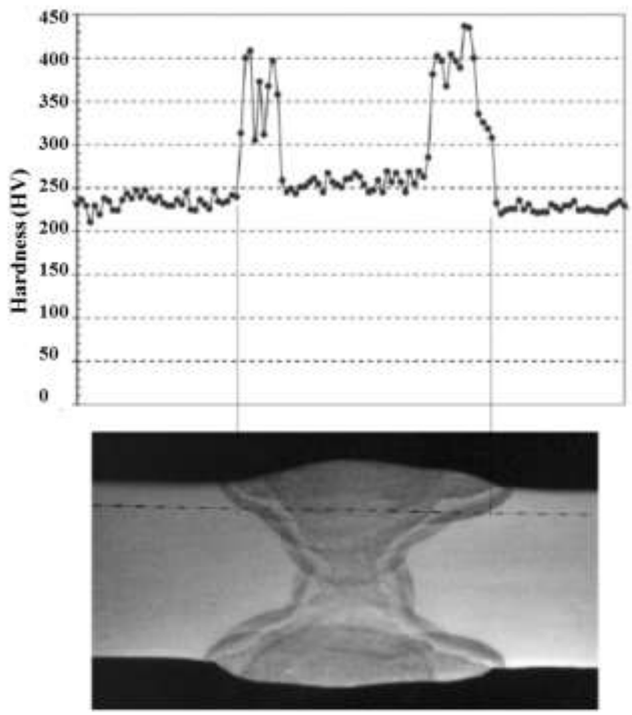

Figure 5: Hardness variation across base metal, HAZ and weld metal regions [13]

Zhu *et al*. investigated the correlation between hardness, microstructure and strength between HAZ of two dissimilar metal joint in 2010. The two dissimilar metals were two types of rotor steel. The two metal parts were welded together by multilayer tungsten inert gas (TIG) technique and submerged arc welding (SAW) techniques. Both micro-hardness and nano-hardness were measured and microstructure of the weldment was observed. In this experiment the largest hardness value was found at the fusion line where the HAZ starts and hardness gradually decreased to the BM side. Zhu et al. used Tabor's and Cahoon's proposal which presents the relationship of micro-hardness with ultimate tensile strength and yield strength respectively. The ultimate tensile strength (UTS) and yield strength (YS) shows a good correlation with micro hardness i.e. highest value of UTS and YS were found at the fusion line (starting of HAZ) and gradually decreased to the BM side [14].

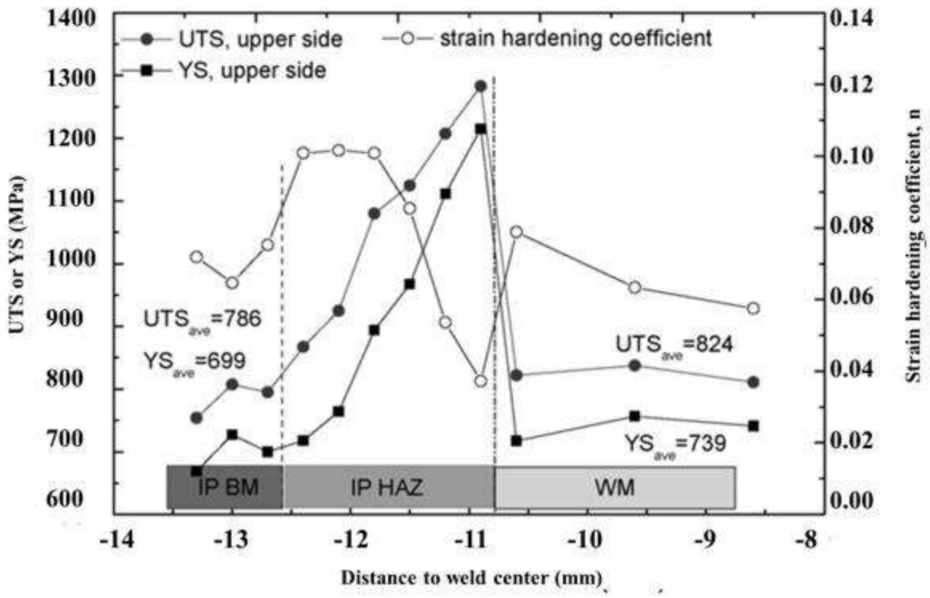

Figure 6: UTS, YS and strain hardening distribution [14]

Reddy *et al*. also made an investigation to assess the mechanical properties of two dissimilar weldments in 2013. In this study gas tungsten arc welding (GTAW) was used to join two dissimilar metal AISI 4140 and AISI 316. Two types of weldment were used: one was autogenous weld and another was welded with filler metal ER309L. In this case microscopic examination, tensile and hardness test were performed to analyze the weldment for their mechanical property. In the microscopic observation, there were clear difference between parent metal and HAZ due formation of the martensite at the HAZ of AISI 4140 in types of weld. In the autogenous weldment carbide formation was witnessed at the HAZ of AISI 316 side. The hardness profile demonstrated maximum hardness at the HAZ of AISI4140 side in both types of weld and also the weld zone of autogenous weldment. The tensile testing result of the both specimen showed that failure occurred at the BM side of AISI 316. The tensile testing result indicated higher strength in both type of welds and strength of both types of welds were comparable with the AISI 4140/AISI 316 BM [15].

Some researchers were also done some investigation on the Poisson's ratio distribution across the weldment. Lee et al. investigate this Poisson's ratio effect across the weldment in 2011. Previously immersion ultrasonic testing method was used for measuring longitudinal and transverse wave speed. But in this work focused transducer and normal transducer were used a scanning results were compared along with the Poisson's ratio scanning and direct Vickers hardness test. The used specimen was a double V-grooved welded steel plate of SM490 BM. Here, CO_2 welding method is used. The specimen width and thickness was 75 mm and 20 mm respectively. This study implied that HAZ has lower Poisson's ration and lower Vickers micro-hardness value [16].

Kabir *et al.* investigated the local and global tensile behavior of laser welded Ti-6Al-4V alloy at different welding speed and defocusing distance. In this analysis, digital image correlation (DIC) technique was used. The specimen thickness was 5.1 mm and Ti-6Al-4V alloy sheets are autogenously welded with laser power 4 kW, defocusing distances -1 mm or -2 mm and also welding speed from 0.75 m/min to 2.0 m/min. The Young's modulus, yield stress and maximum plastic strain value of the weldment were evaluated in this study. The significant findings of this study were i) constant overall yield strength and Young's modulus over all the welding speed and defocusing distance ii) higher Young's modulus and yield stress in the WM zone compared to the BM and lower Young's modulus and yield stress in the HAZ compared to the BM [17].

In 2014, Saranath *et. al* studied the characterization of different zones in the weldment using digital image correlation (DIC) technique. In this work, they investigated different mechanical properties such as Young's Modulus, Poisson's ratio, yield stress etc. The Vickers micro-hardness test was also done to find the micro-hardness value throughout the weldment. Here, butt welded joint of mild steel was used. The welding technique was gas metal arc welding (GMAW). The experimental result implied that the highest hardness was found at FZ and hardness value gradually decreased to the BM. The lowest hardness value was found at the BM. Young's Modulus result implied that there was a decrease in the E value from the BM to the FZ. Poisson ratio was highest at the HAZ region [18].

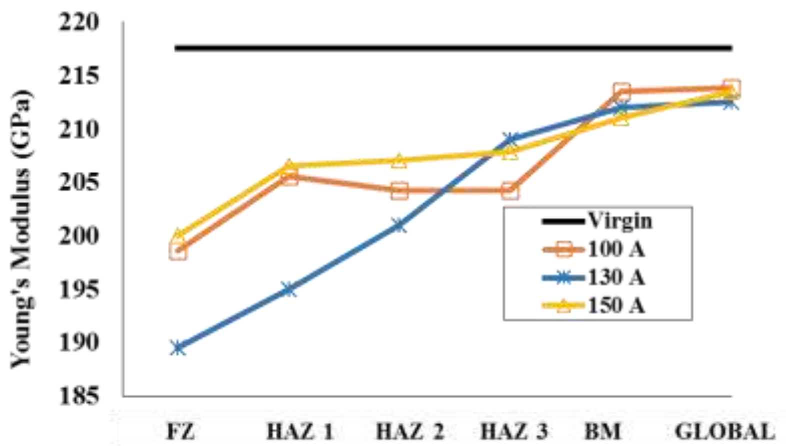

Figure 7: Young's Modulus Variation across the weld zone [18]

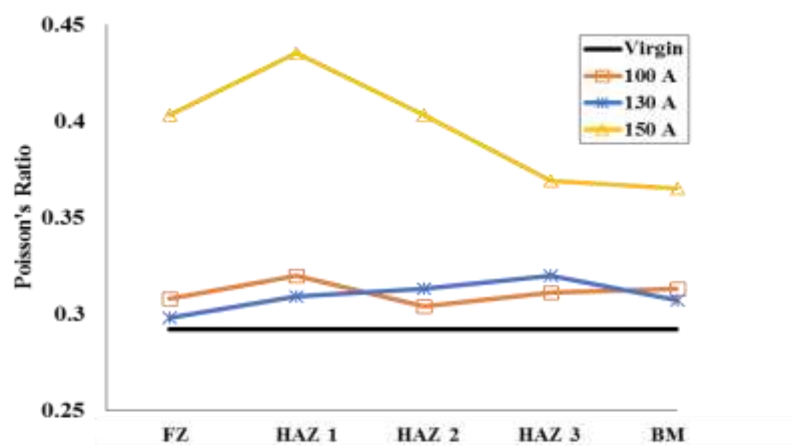

Figure 8: Poisson's ratio variation across the weld zone [18]

Literature reviews suggest that the mechanical property across the weldment does not follow any specific trend. This change varies with type of BM, type of welding process etc. The change in the mechanical property in the weld WM/FZ and HAZ depends significantly on number of factors [19] [20] [21] . The parameter that affects the properties of FZ are mainly as follows [20]:

a) Chemical composition of BM and filler metal
b) Preheating and Heat input
c) BM Thickness
d) Weld joint geometry
e) Electrode Size and number of welding sequence

The HAZ properties are influenced by the following factors [20] [21]:

a) Chemical composition and microstructure of BM
b) Preheating and Heat Input
c) BM thickness
d) Weld joint geometry
e) Number of welding sequence

2.3 Finite Element Modeling of Welded Joint

In the past there are very few works where researcher considered welding joint in the finite element model for stress analysis. This reason significantly created difference between the model behavior and real life behavior of a structure in terms of their dynamic characteristics. This type of inaccuracy in the prediction of model behavior sometimes creates significant issue in the long run. But in the recent year’s researchers have realized the importance of this issue and some interesting research works have been done on the finite element modeling of welded joint. But every study has their specific objective and different way of modeling.

In 1978 Kurtz *et al*. conducted a study on FEA of welded structure. The objective was to anticipate the thermal history of a welded joint structure and to offer a reliable method for weld joint strength optimization. To meet this purpose a computer model was developed based on finite element method. Simple triangular elements were used, specific heat and thermal conductivity were included as function temperature and latent heat of fusion, convection and radiation were incorporated. The result indicated the cooling metal adjacent to weld pool as the critical metallurgical area [22].

Now a days a number of FEA software is gaining popularity such as. ANSYS, MSC Nastran, ABAQUS etc. Some of these software`s have some modeling technique which represents specific type of weld. As per Fang *et al*. report, MSC. Nastran has developed a connector element to represent the load transfer in seam weld and spot weld connections. This weld connector model has physical stiffness. This element can connect to vertex shell points, two surface points and a surface path and a vertex shell points. The user has the advantages to use this for high performance analysis without the generation of explicit constraint. Several analyses on the large automotive model were conducted to prove its efficiency and accuracy [23].

Samhan *et al*. in 2003 studied to predict the strength of weld-bonded joint. They also included resistance spot welded joint and adhesive bonded joint for comparison purpose. In this work finite element technique was used. Three finite elements models were developed (spot welding, adhesive bonded and weld-bonded model) with constrains, loading condition and appropriate material properties. The meshes were generated in GID preprocessing program and Calsef FE program was used for finite element computation. Calsef FE program was an internal module of GID. GID is widely used in structural engineering for data and result generation for linear and nonlinear problems. The result showed concentrated stresses at the both ends of welding nugget in spot-welded joints [24]. Welding nugget is described as a round joint which is generated during the welding of overlapping pieces of metal by the application of electric current and pressure at small point. This creates a pool of molten metal which rapidly cools and solidifies and forms welding nuggets [25]. For weld bonded joint, the stresses are generated at the overlap region as well as both ends of the nuggets. Compared to the major principle stress developed in the weld-bonded joint and adhesive bonded joint, the major principal stress generated in the spot-welded joint was five to six times [24].

Chee *et al.* conducted an analysis to present an appropriate weld model using finite element method in 2007. At first they developed the three-dimensional finite element model of two single plates and validate them using modal analysis. Then a single T-joint of a simple structure was generated by joining two plates that represents arc welded joint. A commercial finite element software ABAQUS/CAE (Computer Aided Engineering) was used in this study. For single plates and T joint analysis two modeling element was used; one was solid and another was shell element. A solid element generally consists of tetrahedral (Tet), hexahedral (Hex) and wedge elements. A shell element comprises of quadrilateral (Quad) and triangular (Tri) elements. Both the models were validated for its natural frequency and its mode shape found in experimental model analysis of single plate and T joint. The result showed that Quad-4 and Hex-8 gave better match compared to the other types of element in case of single plate analysis. From T-joint analysis of shell and solid based model, it was found that the Hex-8, Tri-3, Quad-4 and Tet-4 model of solid based model were suitable to represent welded joint as these produces relatively quite small error. The result also indicated large error for perfect joint. One of the interesting results was found when the researchers tried to improve the accuracy of solid T model by changing Young's modulus. It showed in this study that when the Young's modulus was changed from 207 GPa to 530.35 GPa then the model gave much lower error [26].

In 2008, Anca *et al.* worked on the simulation of fusion welded joint using finite element method. The proposed model considered temperature dependent thermos-physical properties, moving heat source, elasto- plasticity and non-steady state heat transfer. In this study, it is considered that thermal problem is not combined with mechanical problem. The thermal analysis was done separately and prior to mechanical analysis. The thermal history was the basis of mechanical problem. The resulted finite element method model was used to solve the residual stress state of a butt welded joint [27].

In 2009 Marin *et al.* focused on the fatigue design of the welded structure based on finite element method. Generally, there are several methods for the fatigue design of a welded structure such as hot spot stress method, nominal stress method or local approach. Each of them has some limitation with for finite element modeling. In this study, structural stress approach is used for finite element modeling which is basically based on nodal forces. This method can be useful for the fatigue assessment of complex welded structure. According to this work the main characteristics of his technique were accurate crack position, mesh insensitivity and prediction of failure life [28].

Malikoutsakis *et al.* attempted to do finite element modeling of a complex welded structure by using Effective Notch Stress Concept in 2009. This concept presents a comprehensive view of welded structure under the fatigue load. Here the local maximum stress is measured in linear elastic weld model where true notch is replaced by fictitious notch. Notch radius depends on the thickness of the parent material [29]. This study focused on the modelling technique and element number decrease concept by using ANSA. The proposed modeling provided good match with the experimental result for complicated stress state. This avoided possible singularities near critical zones. It offered relatively small solution time as the number of element is low. Another important feature of the model was that it was consisted mostly hexahedral elements at the stress area. This model can be adapted for complex geometries also. Another important thing that is mentioned by the researcher that the standardization of this modeling technique is still ongoing and not fully verified yet [30].

In 2012 Hyoung-Bo Sim also used effective notch stress concept for the evaluation of fatigue performance of welded joints in steel bridge deck. This investigation was conducted on orthotropic steel deck, which is widely used for long and medium-span bridges. This type of structures have expected to various types of fatigue related problem specially in rib-to deck welded joint. As this type joints are subjected to local secondary deformation so this is very susceptible to fatigue. In this study finite element model was developed by using finite element analysis software ABAQUS. The global model was developed by using 3-D shell element model. By taking the boundary condition from the main global model a sub-model was generated using solid element. The advantage of this sub-model was that it can evaluate effective notch stress at the root and toe of the weld joint. The result demonstrated that the maximum notch stress location was the upper side the weld root notch. So this indicated that the cracks are likely to propagate in to the deck plate. This FEA result provided a good match with the experimental crack pattern during the fatigue test [31].

In 2014, Øyvind Sæbø Fagnastøl assessed different weld fatigue approach and worked on the verification of effective notch stress approach [32].

The study of Kang *et al.*is focused on the load estimation method of welded joints using finite element method. This research provided different method to model welded joint and to generate the weld load from FEA result. The discussed methods were stress traction method, maximum nodal load method and spring element modeling method. For the FEA, ANSYS 10 program was used. Shell element model was used for FEA. Among the three methods stress traction method gave the most reliable result. This study recommended further analysis on spring element method for overall structure behavior as well as for weld load [33].

Mhetre *et al.* focused on to develop a reliable welded model to represent welding process using finite element method in 2012. This study mainly aimed to present the physical behavior of the welding process in numerical model. To comply with this accuracy of the model and computational time needed to be adjusted. This study used ANSYS finite element software. Element birth and death technique was used to model the welded joints which demonstrate the melting of the material. The used material properties were temperature and phase dependent. The result gave an overall idea of welding joint and its mechanical aspects [34].

Kassab's *et al*. study was on finite element modeling of seam welded T joint with a V chamfer preparation. This case the objective was to predict the distortion, deformation and residual stress which arise from the welding process. Here the experimental analysis was conducted to validate with finite element model. The element 'birth and death' technique was used to represent welding process in ANSYS software. Temperature dependent non-linear material properties were considered in the simulation process. The finite element model results were compared with the experimentally obtained results in the welding laboratory. The finite element result showed a good match with the experimental result in terms of residual stress [35].

Recently in 2015 Wei *et al*. researched on the regional mechanical properties of the HAZ of laser welded steel joints. Thermocouple was used to measure the thermal histories of different HAZ area during the welding. This was applied to the thermal simulation. The result implied that the HAZ properties are sensitive to the distance from the fusion line and these results in different microstructures as well as mechanical properties. These mechanical properties were applied to the finite element model. ABAQUS was used to model the welded joint. The numerical result exhibited a good match with the experimentally obtained tensile testing result [36].

Literature review suggests different technique of modeling welded joint were conducted in order to develop a reliable welding model which can predict the welded joint behaviour. The various research methodologies are ongoing in this field.

CHAPTER 3

METHODOLOGY

3.1 Workflow Outline

This research has two major parts. The first part was associated with the experimental analysis and FEM modeling of a simple arc welded sample. A real arc welded multi-passenger bus structure was used in the second part for experimental studies and FEM model generation. In the first part, ASTM standard arc welded sample was used for experimental studies. In this stage, the width of the HAZ was measured by observing the microstructure of weldment under an optical microscope. Then tensile testing of another similar ASTM standard sample was performed to find out the mechanical properties of the HAZ and BM zone. The FEM model of ASTM standard specimen has been developed and validated using these obtained experimental results. Then, in the second part, the experimental analysis of a window pillar structure of a real multi-passenger bus was performed under the braking load condition. The braking load condition is one of the critical loading conditions of a bus structure. The window pillar structure was manufactured by same welding technique and condition like ASTM standard specimen. Then, the FEM model of window pillar structure has been developed based on the width and mechanical properties i.e. Young's modulus of the HAZ obtained from ASTM standard sample and mechanical properties i.e. Young's modulus of the BM zone obtained from the tensile testing of BM sample of window pillar. Both the window pillar and the ASTM standard specimen were prepared by gas metal arc welding process (GMAW) of same grade of stainless steel with same filler material. For this reason, the HAZ width and Young Modulus value of ASTM standard specimen are similar with the ones of the window pillar structure and was hence used in the modelling of window pillar. The validation of the developed FEM model is done by comparing the FEA results with the experimental results under the braking load condition. The full work can be summarized as the following workflow diagram:

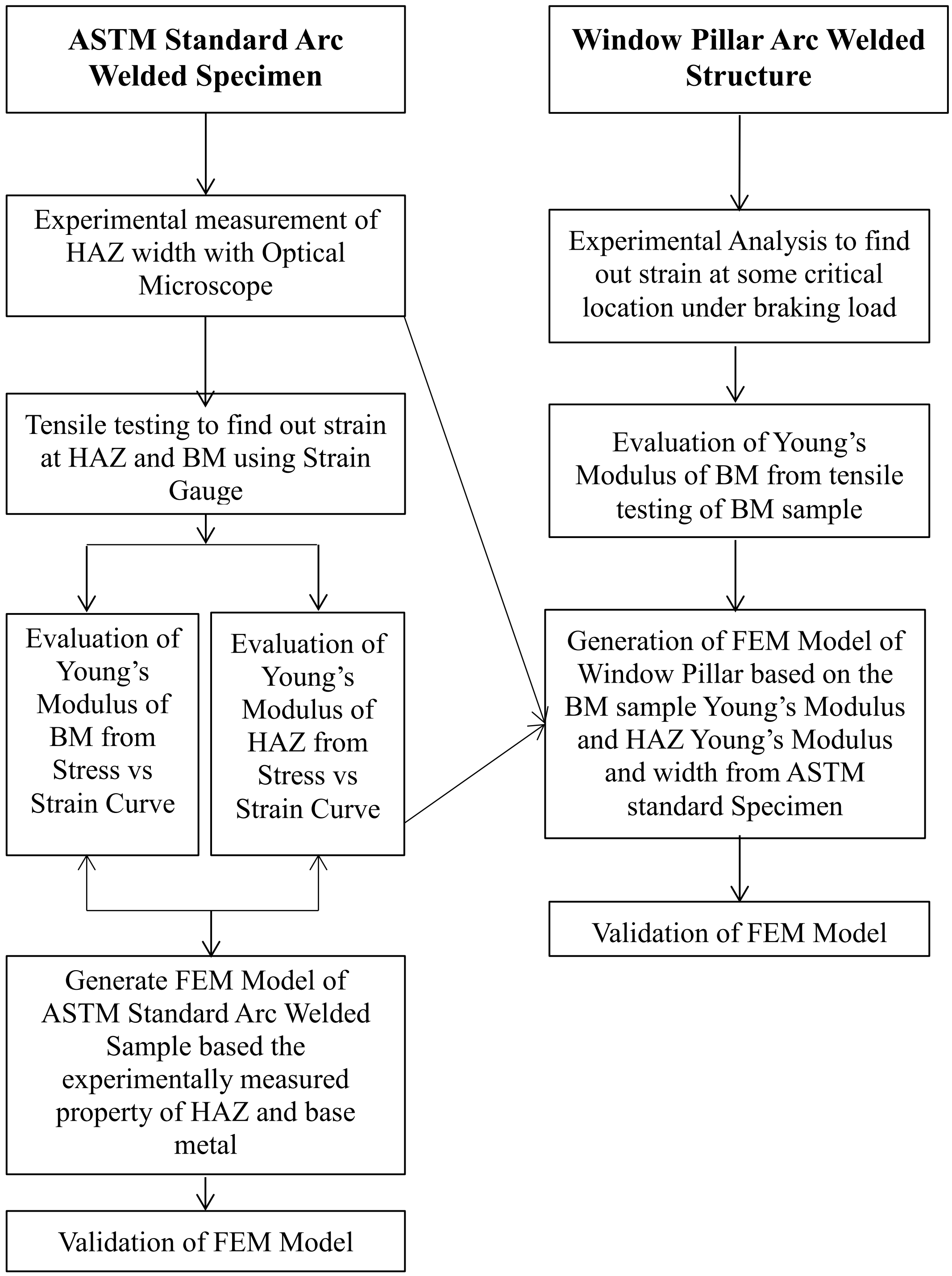

Figure 9: Work Flow Outline of the Research

3.2 Experimental Analysis

The details experimental procedure of the ASTM standard specimen and window pillar specimen are described below. The experimental testing results are used to generate and validate the FEM models.

3.2.1 ASTM Standard Specimen

In this study, two arc welded ASTM standard samples were used for experimental analysis. The dimension and shape of both the samples were produced according to the ASTM standard. The samples were manufactured by Gas Metal Arc Welding (GMAW) process under same welding conditions i.e. same heat input and wire speed. The overall length and width of the sample was 180 mm and 24 mm respectively while gage length and width was 80 mm and 12 mm respectively. The thickness of the specimen was 3 mm. The base material was SS41003 while the filler material was AWS ER 308L. Therefore, both the samples are exactly the same with dimensions, geometry, welding conditions and materials. The first sample was used for microscopic observation while tensile testing was performed on the second one.

Figure 10: ASTM Standard Arc Welded Specimen

3.2.1.1. Microscopic Observation and Measurement of HAZ width:

The characterization of microstructure of the weldment is very important helping us to understand the weldability of materials. It is also very significant to correlate the microstructure and mechanical properties of the welds. The microstructures of HAZ and FZ are complex. Due to rapid heating and cooling in a given thermal cycles, this complexity arises. There are different types of techniques available for characterization of welding microstructure such as optical microscopy (OM), transmission electron microscopy (TEM), scanning electron microscopy (SEM), orientational imaging microscopy (OIM) and X-ray diffraction (XRD) etc. [37].

Optical Microscopy is generally used to characterize a structure or specimen by revealing its phase boundary, grain boundary etc. It is used to characterize the solidification of microstructure [38] and very effective to evaluate the details of a weld microstructure as well. The use of optical microscopy can reveal different microstructures of a BM, HAZ and FZ. This will help to measure the HAZ width by observing its microstructural difference from the BM and FZ. Sometimes electron microscopy is also used to obtain finer details of the microstructure of weldment [37].

In this research, optical microscopy was used to see the microstructure of the weldment and also to find out the width of the HAZ. To determine the microstructure, proper preparation of the metallographic sample is quite important. Preparation of metallographic specimen is a step by step process. The process consists of cutting/ sectioning, mounting, coarse grinding, medium and fine grinding, mechanical polishing, etching and microscopic examination. To reveal the accurate microstructure, the sample was kept clean and preparation processes were carried out carefully [39].

Electric discharge machine (EDM) was used for cutting one of the ASTM standard samples into a required dimension. ASTM standard sample was cut into a 24 x 6 x 3 mm section shown in

Figure 11. The sectioning was done in such a way that it represents the feature of the main ASTM standard sample and contained all the information required to investigate.

Figure 11: Sectioned ASTM Standard Sample

Mounting of the sample is required to allow them to handle easily. The chance of damage likely to happen to the sample itself is also minimized. The sample was mounted in plastic and compression type molding was applied to encase the sample. In this study, Bakelite was used as molding materials. This is one of the commonly utilized molding materials.

Next step was coarse grinding. The coarse grinding is generally performed to produce initial flat surface required for subsequent grinding and polishing stages. In this study coarse grinding was accomplished using 140 grit abrasive paper by electrically powered disks/wheel (Figure 12) in wet condition. The flow of water needed to be adjusted to obtain a good film of water. Excessive water might cause a spray when it is contacted with the sample.

After coarse grinding, the sample was ready to move for medium and fine grinding. The sample was washed thoroughly before proceeding from coarse grinding to medium and fine grinding. This was done carefully because that debris from one step can contaminate next step.

During medium and fine grinding process 320, 600 and 1020 grit abrasive paper was used in successive steps. The grinding rate was decreased steadily from one step to the next. Wet grinding was applied in medium and fine grinding steps to avoid the side effects of heating. After grinding, the sample was rinsed thoroughly before proceeding to polishing.

Figure 12: Machine used for Grinding

6-micron aluminum oxide was used at the first stage of mechanical polishing. Initially, the sample was held at one position of the wheel of the polishing machine (Figure 13) without rotation until most of the previous grinding marks were removed. Then it was rotated slowly counter to the direction of wheel rotation. The sample was washed to proceed for 1-micron aluminum oxide stage. This stage was carried out in the separate polishing wheel.

Figure 13: Polishing Machine

During the first stage, the applied pressure was medium compared to the second stage. After finishing of mechanical polishing, the surface of the sample got a mirror like finish and free of scratches. The sample was washed and dried before proceeding to etching. The surface of the sample should not be touched.

Etching was generally used for highlight and identifies microstructural features or phase present. The chemical etching is usually done by applying an appropriate solution to the surface of the sample for several seconds or minutes. In this study, 10 g of oxalic acid in 100 ml water was used as etchants. Around 30s was required for proper etching. After etching the sample was washed under water and then rinsed with alcohol and dried.

Figure 14 : Prepared Sample for Microscopic Observation

Now the sample was ready for microscopic observation (shown in Figure 14). The sample should not be touched, wiped or swabbed before microscopic observation

After the sample preparation, it was examined under the optical microscope (Figure 15) to see the microstructural difference in the weldment to find out the HAZ width.

Figure 15: Optical Microscope used for Microscopic Observation

3.2.1.2 Tensile Test

A tensile test is one of the most basic mechanical tests that is performed on material. This type of tests is widely used but it is simple, fully standardized and inexpensive. It gives a quick idea about how a material will react to applied tensile force. Tensile tests are generally used to evaluate the Young's modulus, elastic limit, elongation, proportional limit, and reduction in area, tensile strength, yield strength, yield point and other tensile properties [40].

Tensile testing machines are either hydraulic or electromechanical. The principle difference lies in the load applied method [40].

During the tensile test, the specimen is mounted in a tensile testing machine and subjected to tensile load. If the specimen is pulled until it breaks (similar setup like Figure 19), then it will give a good and complete tensile profile. Figure 16 shows a typical curve for a material subjected to tensile load. The point of failure is termed as Ultimate Strength or UTS on the chart. For most of the materials, the initial portion of the curve is linear and the slope of this region is termed as elastic modulus or Young modulus [41].

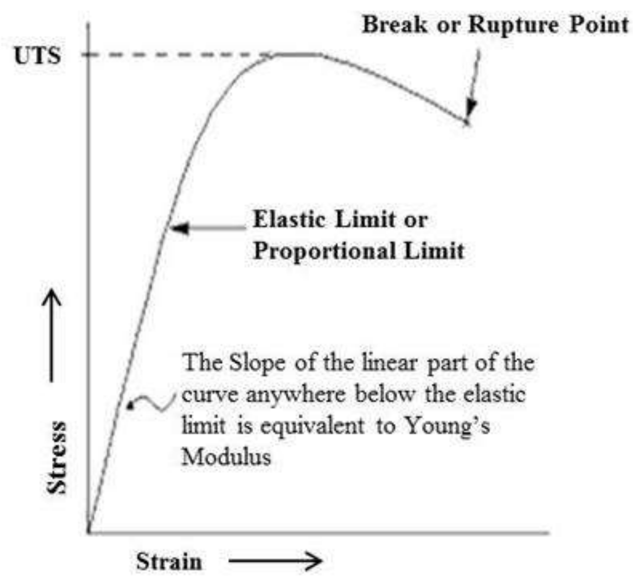

Figure 16: Typical Curve for a Material Subjected to Tensile Load [41]

Young's Modulus, $E=\sigma/\epsilon$ (1)

Here, σ = Engineering stress or nominal stress

ϵ = Engineering strain or nominal strain

In this linear elastic region, the ratio of the lateral strain to axial strain is called Poisson's ratio.

Poisson's Ratio, $\nu=-\varepsilon_y/\varepsilon_x$ ((in an x-direction tensile test) (2)

Here, ε_y= Lateral Strain/Normal Strain in y-direction

ε_x=Axial Strain/ Normal Strain in x-direction

Among the several methods of measuring strain, the most common is with a strain gauge. In this work 3D (rectangular rosette) strain gauge has been used. A series of equations were used to convert strain gauge data into the required normal and principle strain [42].

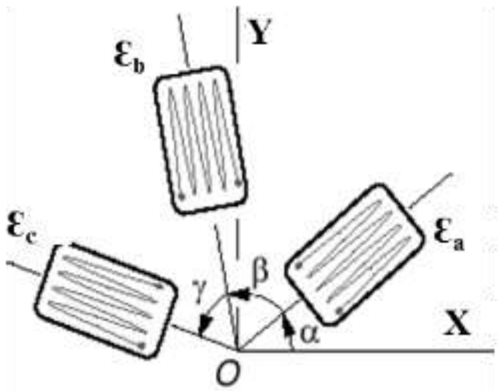

Figure 17: Strain Rosette for Strain Measurement

In the above Figure 17, it is shown that a strain gauge is attached on the surface of the specimen with an angle α from the X-axis. The internal angle of the rosette is β and γ. If the measured strains from the strain gauge are ε_a, ε_b and ε_c then the normal strain and shear strain can be calculated from the following equations [42],

$$\varepsilon_a = \frac{\varepsilon_x+\varepsilon_y}{2} + \frac{\varepsilon_x-\varepsilon_y}{2}\cos 2\alpha + \frac{\gamma_{xy}}{2}\sin 2\alpha \quad (3)$$

$$\varepsilon_b = \frac{\varepsilon_x+\varepsilon_y}{2} + \frac{\varepsilon_x-\varepsilon_y}{2}\cos 2(\alpha+\beta) + \frac{\gamma_{xy}}{2}\sin 2(\alpha+\beta) \quad (4)$$

$$\varepsilon_c = \frac{\varepsilon_x+\varepsilon_y}{2} + \frac{\varepsilon_x-\varepsilon_y}{2}\cos 2(\alpha+\beta+\gamma) + \frac{\gamma_{xy}}{2}\sin 2(\alpha+\beta+\gamma) \quad (5)$$

Here, ε_x= Normal strain in X-direction

ε_y=Normal strain in Y-direction

γ_{xy}=Shear strain

When $\alpha=\beta=\gamma=45^0$ then the solution of above equations become as follows,

$$\varepsilon_x = \varepsilon_a - \varepsilon_b + \varepsilon_c \quad (6)$$

$$\varepsilon_y = \varepsilon_b \quad (7)$$

$$\Upsilon_{xy} = \varepsilon_a - \varepsilon_c \quad (8)$$

The equations for calculating maximum/minimum principle strains $\varepsilon_{1,2}$ and maximum shear strain $\Upsilon 1.2$ are as follows:

$$\varepsilon_{1.2} = \frac{\varepsilon_x+\varepsilon_y}{2} \pm \sqrt{(\frac{\varepsilon_x-\varepsilon_y}{2})^2 + (\frac{\Upsilon xy}{2})^2} \quad (9)$$

$$\Upsilon_{1.2} = \sqrt{(\frac{\varepsilon_x-\varepsilon_y}{2})^2 + (\frac{\Upsilon xy}{2})^2} \quad (10)$$

The obtained principle strains and shear strain are then used to calculate maximum principle stresses $\sigma_{1,2}$,

$$\sigma_1 = \frac{E}{1-v^2}(\varepsilon_1 + v\varepsilon_2) \quad (11)$$

$$\sigma_2 = \frac{E}{1-v^2}(\varepsilon_2 + v\varepsilon_1) \quad (12)$$

The equivalent or von-mises stresses can be calculated from principle stresses using the following equation,

$$\sigma_{vm} = \sqrt{(\sigma_1 - \sigma_2)^2 + \sigma_1{}^2 + \sigma_2{}^2} \quad (13)$$

In this study, tensile testing was performed with the second ASTM standard sample. During the tensile testing, only one directional load was applied on the sample. A MTS tensile testing machine (Capacity 30 KN) was used for this test (Figure 18.a). The testing was performed at different loadings (250 N, 500 N, 750 N, 1000 N, 1250 N, and 1500 N) within the elastic limit. Two (2) strain rosettes (C2A-06-031WW-350) were used to collect strain data. For each load step, the testing was performed four to five times to check the standard deviation and repeatability of the results. The average value of repetitive results was used for further analysis. A 32-channel data acquisition system (DAQ) was used to collect strain gauge data (Figure 18.b).

a)

b)

Figure 18: a) MTS Tensile Testing Machine (30 KN) b) 32-channel data acquisition system (DAQ)

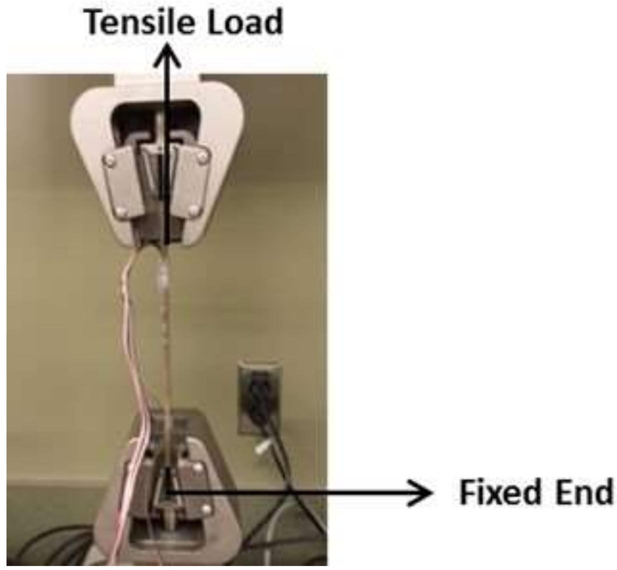

Figure 19: Tensile Testing Setup

The two strain gauges were attached at the bottom of the sample. One strain gauge was attached on the bottom of the specimen in such a way that it covers the HAZ width which was obtained from microscopic observation and another strain gauge was attached on the BM area. Figure 20 shows the strain gauge locations on the specimen.

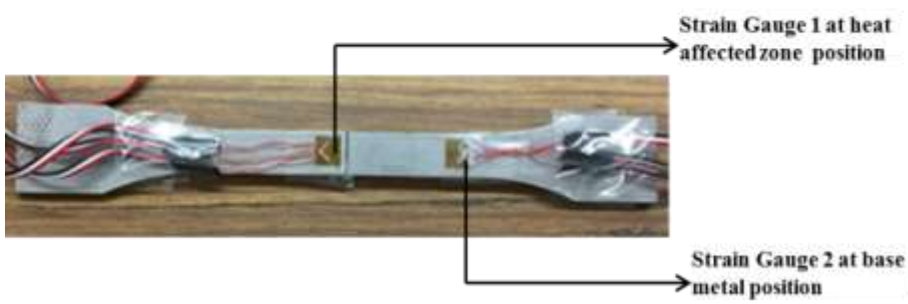

Figure 20: Strain Gauge Location on ASTM Standard Specimen

The stress vs. strain curve was plotted from the experimental results of two strain gauges, which is shown in the next chapter. Young's modulus of HAZ and BM zone was obtained from these curves. Poisson's ratio was also obtained from the ratio of lateral strain and axial strain.

3.2.2 Window Pillar Structure

The next step of experimental analysis involves the testing of a window pillar joint of a real multi-passenger bus structure. This window pillar structure was produced by Gas Metal Arc Welding (GMAW) under the same welding condition which was used for ASTM standard sample. In this structure, the three tubes were joined by the four welds. Two welds are at the front side and two at the back. Figure 21 represents the window pillar structure which is used in this research. The base material of the tubes was SS41003 while the filler/weld material was AWS ER 308L.

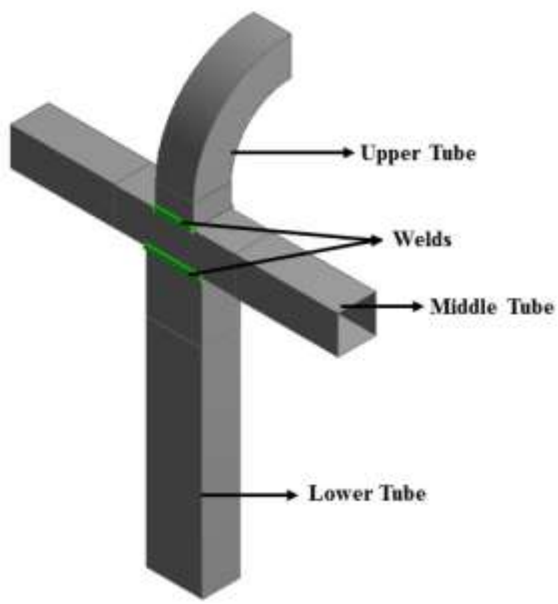

Figure 21: Window Pillar Structure of a Multi Passenger Bur Structure

3.2.2.1 Testing under Braking Load

The experimental analysis on the window pillar joint was performed under a loading condition which represents the braking load condition of the whole bus structure. The braking load condition is one of the critical load conditions of a bus structure. Therefore, this loading condition was chosen for the experiment to find out strain behavior around the welds which are considered to be the critical location of the structure.

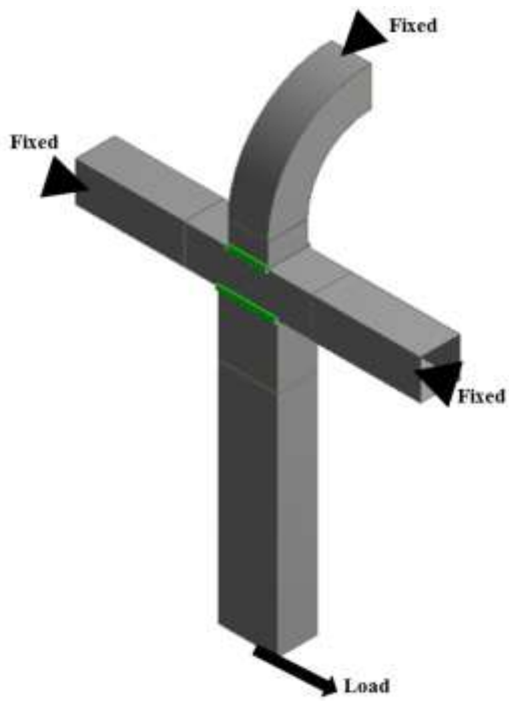

Figure 22: Braking Load Condition of the Window Pillar Structure.

This study was conducted at Industrial Technology Center (ITC). In this work, MTS hydraulic type testing machine was used to apply load. The capacity of the load cell used in this experiment was 10000 lbf or 44.5 KN (approx.). Total six (6) strain rosettes (C2A-06-031WW-350) were used to collect strain data from the window pillar joint. Three strain gauge were attached at the front side and three were attached at the back as shown in Figure 23

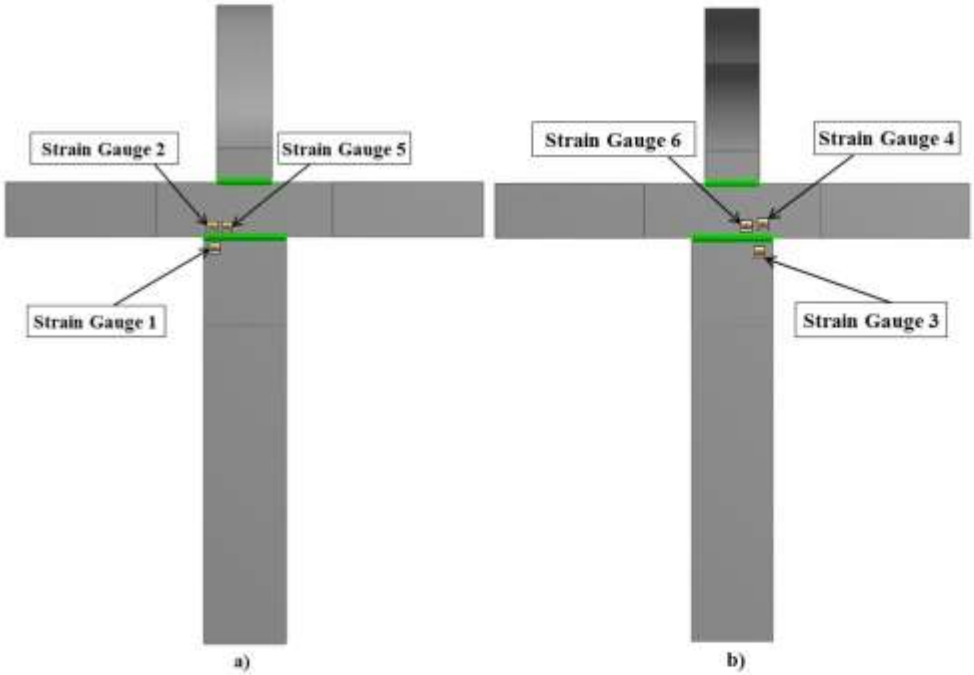

Figure 23: Strain Gauge Location a) at Front Side b) at Back Side

The testing was performed at different loading points (500 N, 1000 N, 1500 N, 2000 N and 2500 N). The load was applied in such a way that it remains within the elastic range of the weldment. For each load step, the testing was performed several times to check the standard deviation and repeatability of the results. The average value of repetitive results of each load step was used for further analysis. In this case, another 32-Channel DAQ system was used to collect strain data which was available at ITC.

In this experiment a part of a commercial vehicle is used, therefore, all the experimental details and pictures are not presented in this thesis due to non-disclosure agreement.

3.2.2.2 Tensile Testing of the Base Material Sample

To determine the mechanical property of the base material the samples of the tubes were tested under tensile testing method. The tensile testing was performed on these tube samples until fracture. The stress vs. strain curve was obtained from the experimental result. From the slope of the stress vs. strain curve, Young's modulus was evaluated. The testing results and the stress vs. strain curve are discussed in the next chapter.

3.3 Finite Element Modeling based on Experiment

In this research, finite element simulation software ANSYS 15 workbench was used for finite element analysis for both the samples. Both the ASTM and window pillar specimens were modeled and simulated as per the standard working procedure of ANSYS 15 workbench environment. The full procedure is a step by step process. The details of the procedure are described below.

3.3.1 ASTM Standard Specimen

At first, Design Modeler of ANSYS 15 workbench was used to create the geometry. In this study, static structural module was used. After developing geometry, the standard procedures i.e. meshing, boundary conditions and loading were applied to do the FEA.

3.3.1.1 Geometry

The first step of finite element modeling is to produce geometry as per the original specimen. The geometry of the ASTM standard sample was developed according to the original shape and dimension of the specimen. The three distinct zones in the weldment were also modeled carefully. The width of the HAZ was given as per the experimentally obtained result. Figure 24 represents developed finite element model of ASTM standard specimen with three distinct zones in the weldment. The full model was developed using solid elements.

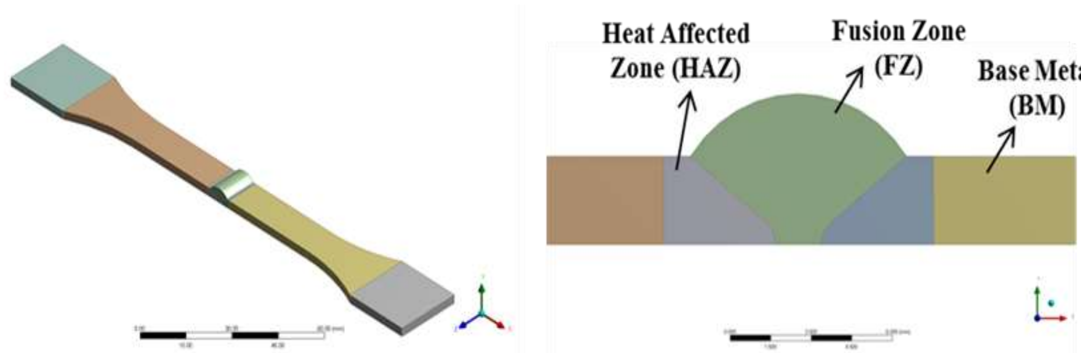

Figure 24: Finite Element Model of ASTM Standard Specimen

3.3.1.2 Meshing

Meshing is one of the most important steps in finite element modeling. The result accuracy and credibility greatly depend on the meshing quality of the model. It is important to have fine mesh around the critical area i.e. FZ and HAZ and coarse mesh around the remaining whole area. The spherical influence method was used to produce fine mesh density in the critical areas. Element size 0.225 mm was used in these critical areas while element size 1 mm was used for the whole model. Hexa Dominant Method was used to mesh the full model. Figure 25 shows the meshing of the finite element model of ASTM standard specimen.

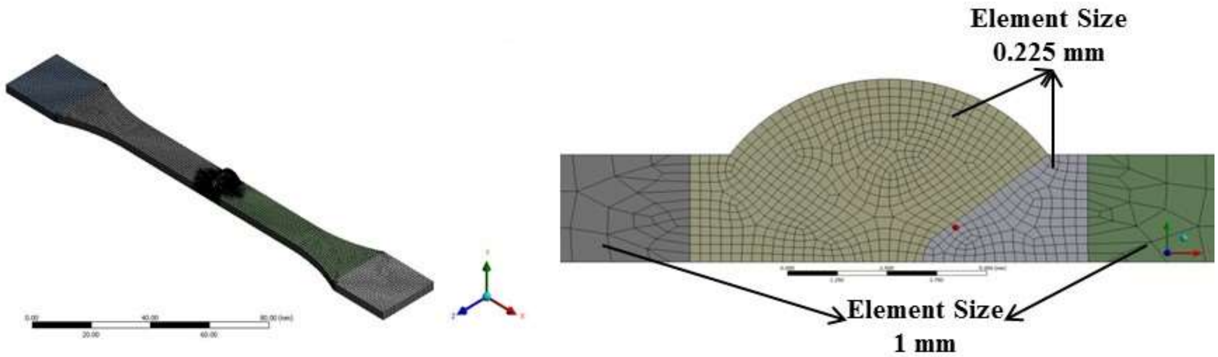

Figure 25: Meshing of finite element model of ASTM standard specimen

To obtain a reliable result, mesh convergence study is necessary. Mesh convergence study has been performed to acquire a satisfactory element size of the mesh which balances the result accuracy and computation efficiency. A mesh is assumed to be converged when a mesh refinement reaches in such a stage that any further refinement negligibly affects the solution. After convergence study, element size 0.225 mm has been taken as the optimum value for the critical areas. Figure 26 shows the mesh convergence result for the ASTM standard specimen.

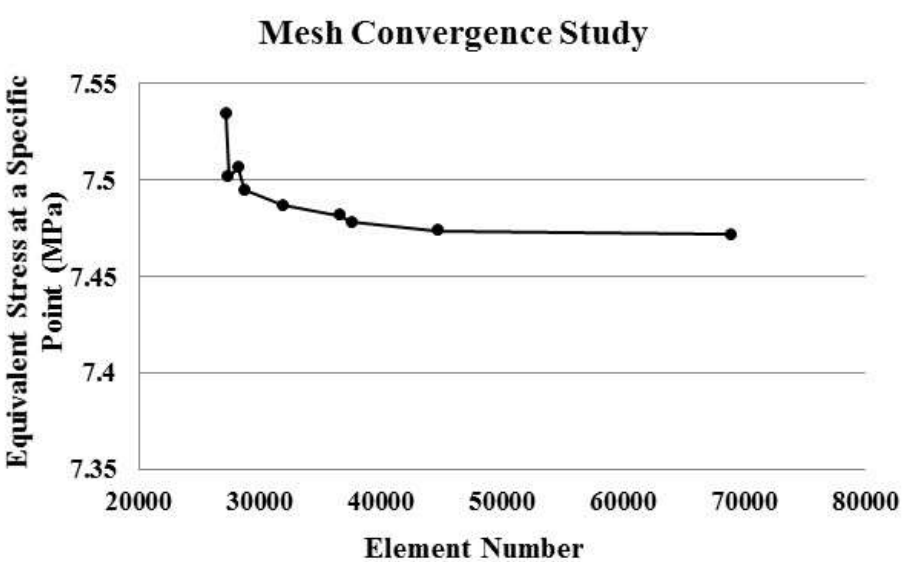

Figure 26: Mesh Convergence Study of FE Model of ASTM Standard Specimen

3.3.1.3 Boundary conditions

The next step of FEA is to set up proper boundary conditions. It is very important that the given boundary conditions represent the real experimental conditions. The applied boundary conditions were given as follows:

a) One end was fixed

b) Force was applied on the other end in X direction shown in figure 24. Displacements in Y and Z directions were zero.

The boundary conditions of the ASTM standard model are shown in Figure 27.

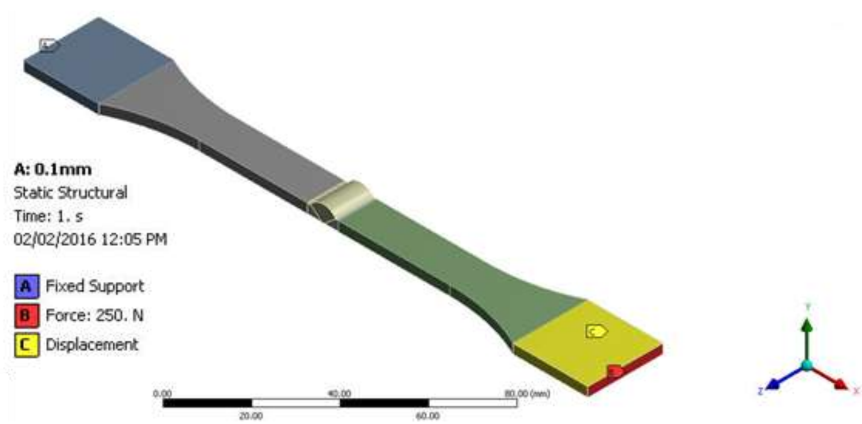

Figure 27: Boundary Conditions of FE Model of ASTM Standard Specimen

3.3.1.4 Material Properties

Assigning of the proper mechanical property is very crucial to obtain an accurate result. In this analysis, the experimental value of Young's modulus and Poisson ratio of HAZ and BM zone obtained from the tensile testing of the specimen has been applied to the finite element model. The Young's modulus of the FZ was used from the literature [43].

3.3.1.5 Simulation

After assigning proper boundary conditions and material properties to the meshed model, the model was ready for simulation. The simulations were conducted at 250 N, 500 N, 750 N, 1000 N, 1250 N and 1500 N load condition to compare the results with experimental analysis.

3.3.2 Window Pillar Joint

To model the window pillar joint a special modelling technique i.e. submodeling technique was used. The reason of using submodeling technique is that this technique is very useful to solve a smaller part of a larger structure with more refined meshes and more accurate results. With the smaller submodel, it is convenient to obtain more refine mesh at the critical region. So, the submodel provides a better result compared to the full model with Coarse mesh. Moreover, the computational time reduced significantly with the submodel. In this technique initially a coarser and faster full model was analyzed. Then a details analysis is performed with the submodel on the regions of interest. For submodeling procedure, it is important to follow that the submodel boundary must be far away from the loading regions and constraint boundaries [44]. The submodeling is performed by the following procedure:

- Create and analyze the initial model
- Create the Submodel
- Perform cut boundary interpolation
- Analyze the Submodel
- Verify results and cut boundary position

In this analysis, Shell to Solid submodeling technique was used. The full procedure was done on

ANSYS 15 workbench where Shell to Solid submodeling transfer key is available. The step by step procedure of shell to solid submodeling is discussed below.

3.3.2.1 Geometry

At first, a full model of window pillar joint was developed. The shape, geometry and dimension of the model was developed in such a way so that it represents the original specimen. In this model only welded part was developed using Solid element and all other parts are developed using Shell element. The geometry of the initial full model is shown in Figure 28.

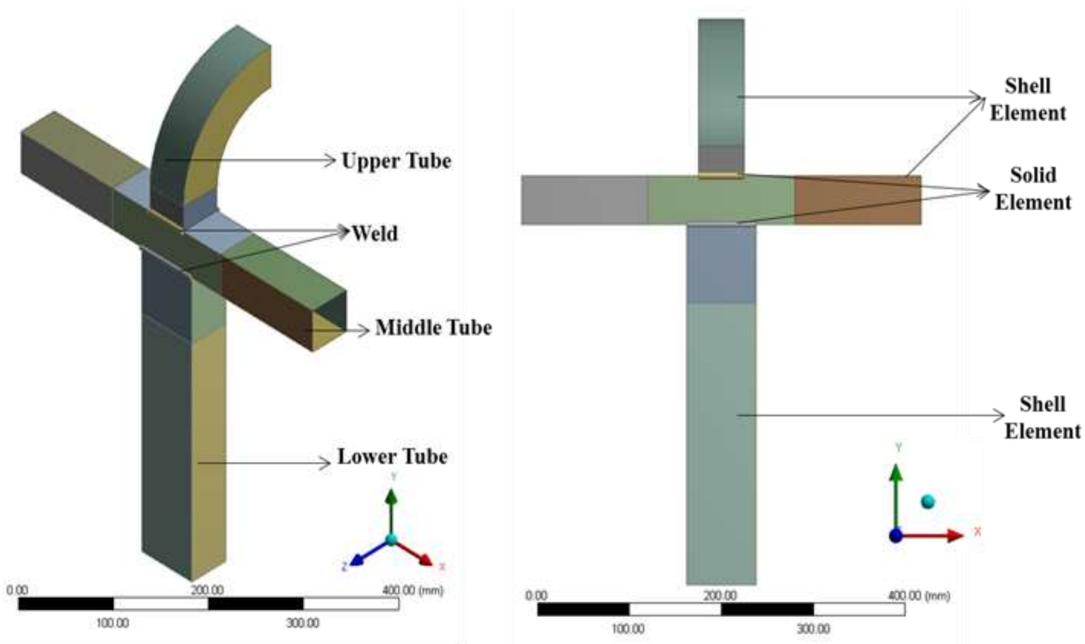

Figure 28: Initial Full Model of Window Pillar Structure

The geometry of the submodel was developed using solid element for weld as well as the other parts of the structure. In this analysis two submodels were developed; one was for front lower weld and another was for the back lower weld. The submodels were built using the same coordinate system which was used for the full model. The submodels regions were selected only around the lower weld because in the experimental analysis all strain gauges were attached around the lower weld. So in this study, the regions of interest are also around the lower weld. In the submodel, HAZ was also created around the weld. Figure 29 represents the geometry of the developed submodel.

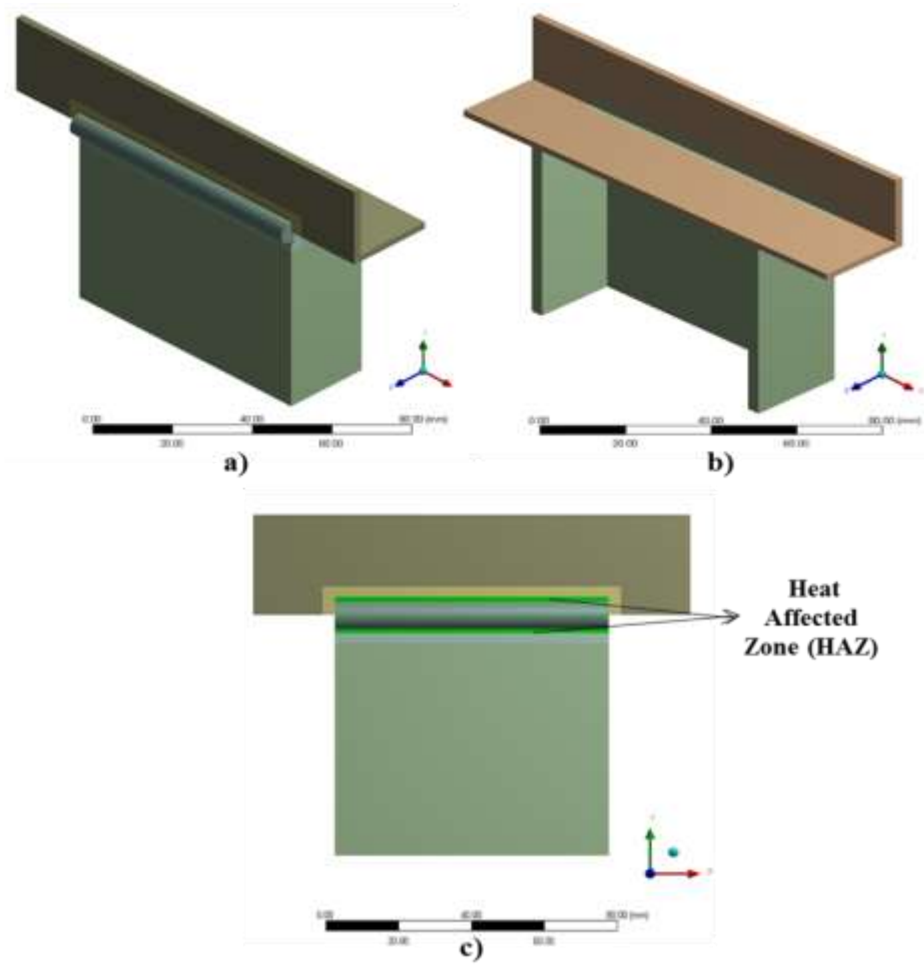

Figure 29: Submodel Geometry a) Front b) Back and c) Heat Affected Zone (HAZ) Location

3.3.2.2 Meshing

The meshing of this type of structure is very critical. In this case also fine mesh was produced around the FZ and HAZ. The spherical influence method was used for the full model to have fine mesh density in these critical areas. For the submodel, the refined mesh was produced around the FZ and HAZ by assigning smaller element size for those areas. Hexa Dominant Method was used to mesh the submodels. The meshed full model and submodel are shown in Figure 30.

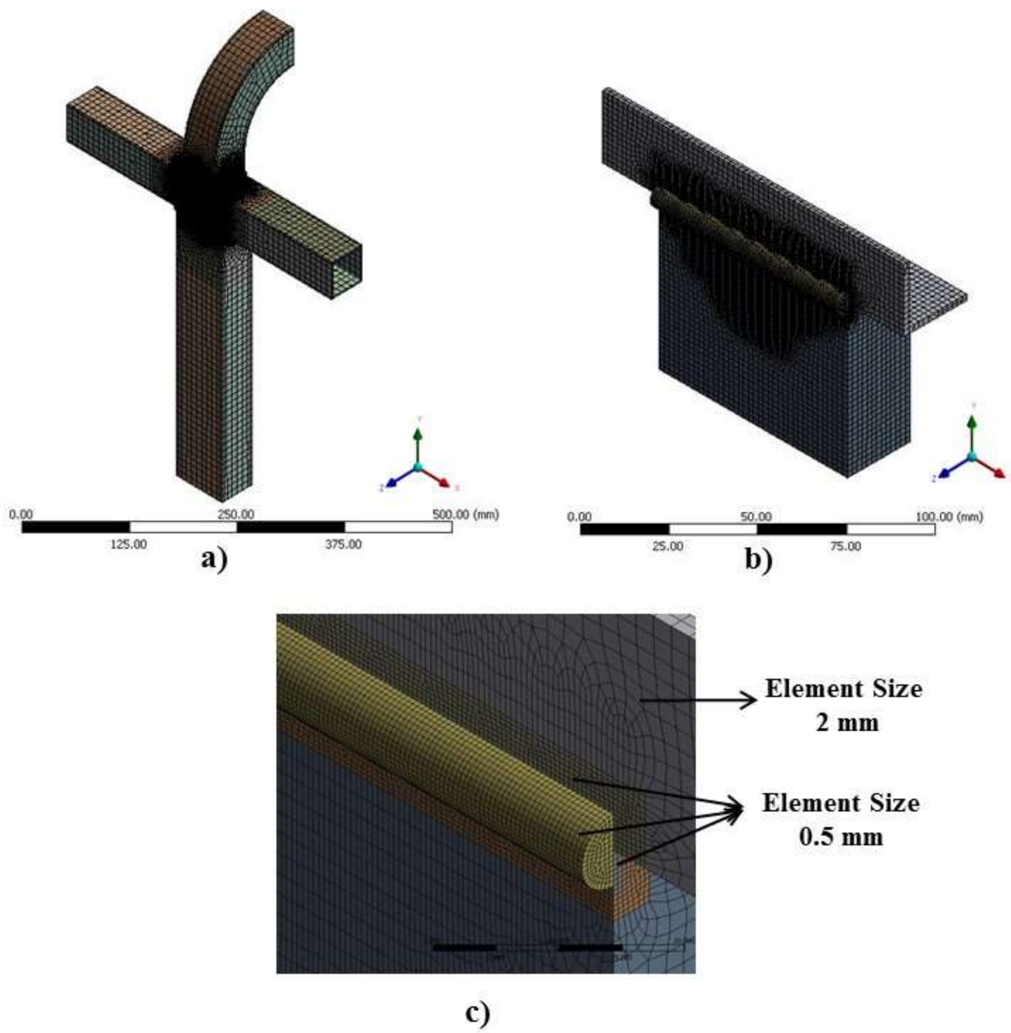

Figure 30: Meshing of a) Full Model b) Submodel c) Critical Region of Submodel

The mesh convergence study was also performed for full model and submodels. For the submodels, more refined mesh was obtained around the weld and HAZ with mesh convergence. This will provide more refined and better results. After the convergence study element size 0.85

mm was taken as the optimum value for the critical areas of the full model where in the case of submodels the optimum value is 0.5 mm for FZ and 0.5 mm for HAZ and around the HAZ. Figure 31 & Figure 32 shows the mesh convergence study for the full model and submodel respectively.

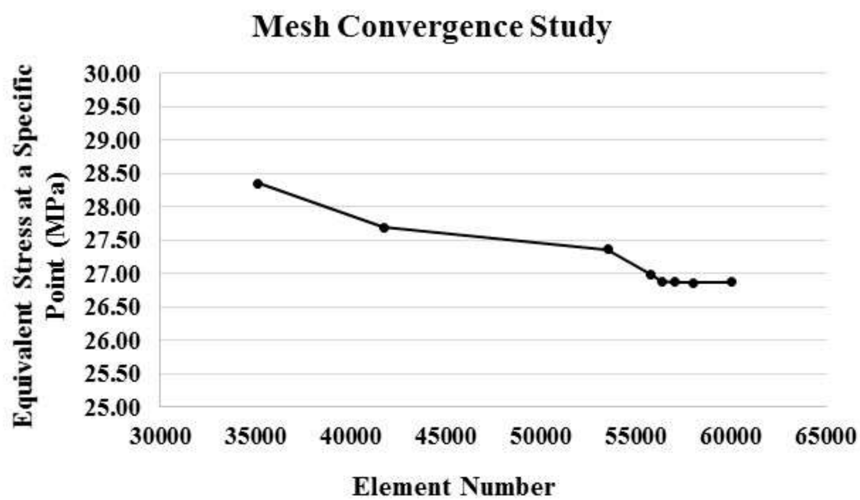

Figure 31: Mesh Convergence Study of Full Model of Window Pillar

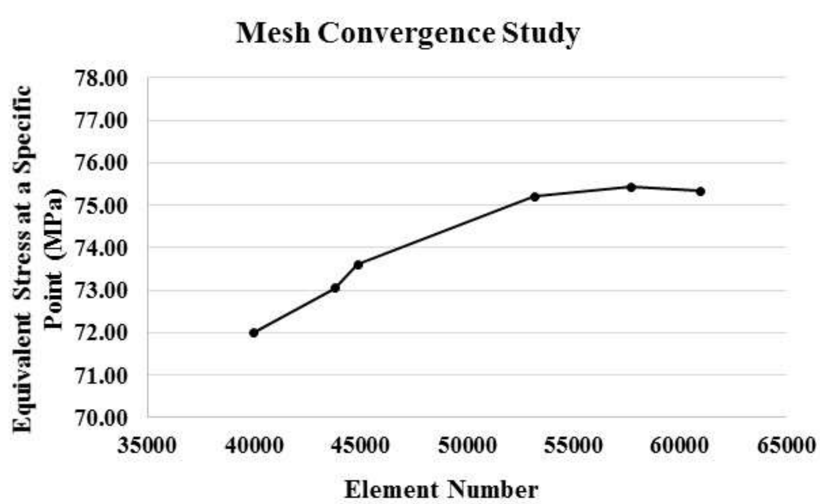

Figure 32: Mesh Convergence Study of Submodel of Window Pillar

3.3.2.3 Connections

The connection between the contacting bodies in a structure is very important. The stiffness of the structure depends on the contact status, whether the bodies are touching or separated. To represent the real behavior of a structure it is necessary to assign accurate contact between the bodies. There are various types of contact behavior available in ANSYS such as bonded, no separation, frictionless, rough and frictional [45].

The full model structure consists of three tubes which are connected by the welded parts. As the welds are bonded with the surface so the contact between the weld and the tube surface was defined as “bonded” type contact i.e. no penetration, no separation and no sliding between faces or edges. Despite the “bonded” connection there might be some flexibility in the connection between the bodies and the target faces [46]. So contact formulation was assigned to these bonded contacts. Figure 33 shows the bonded connections in the full model.

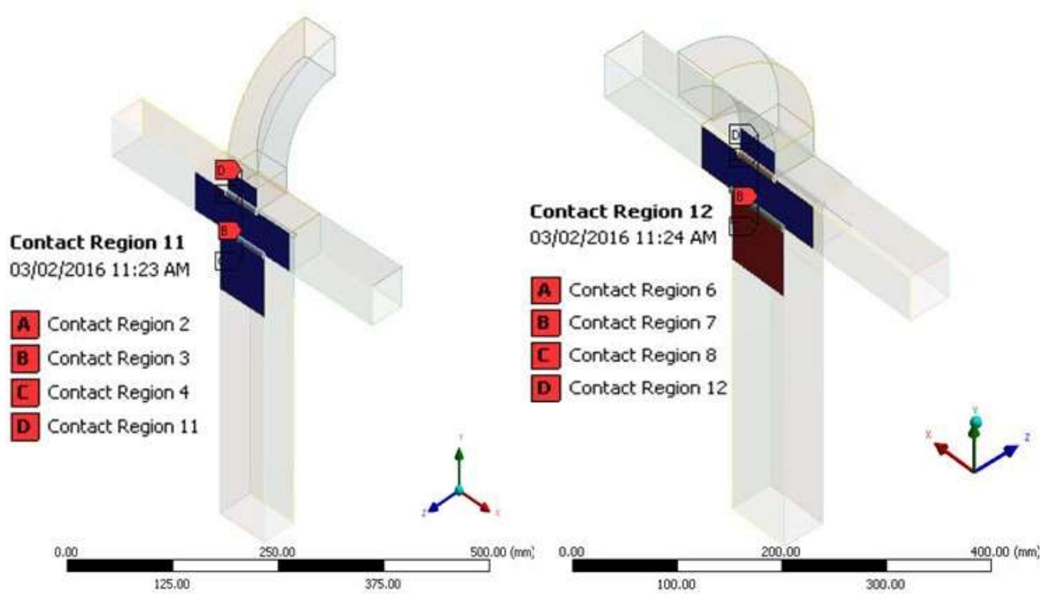

Figure 33: Bonded Contacts of Full Model

For this model MPC (Multi Point Constraints) contact formulation was used. This type of formulation mainly applied to the bonded type contact. By this formulation, degrees of freedom at the nodes on the contact and target faces are eliminated by the constraint equations. This formulation also supports large deformation effects [46].

The contact between the tubes surface was assigned as frictional contact. As the tubes are made of stainless steel so there will be friction between the surfaces. Therefore, frictional contacts were assigned for these connections. The frictional coefficient value 0.75 was used. Figure 34 represents the frictional contact in the full model.

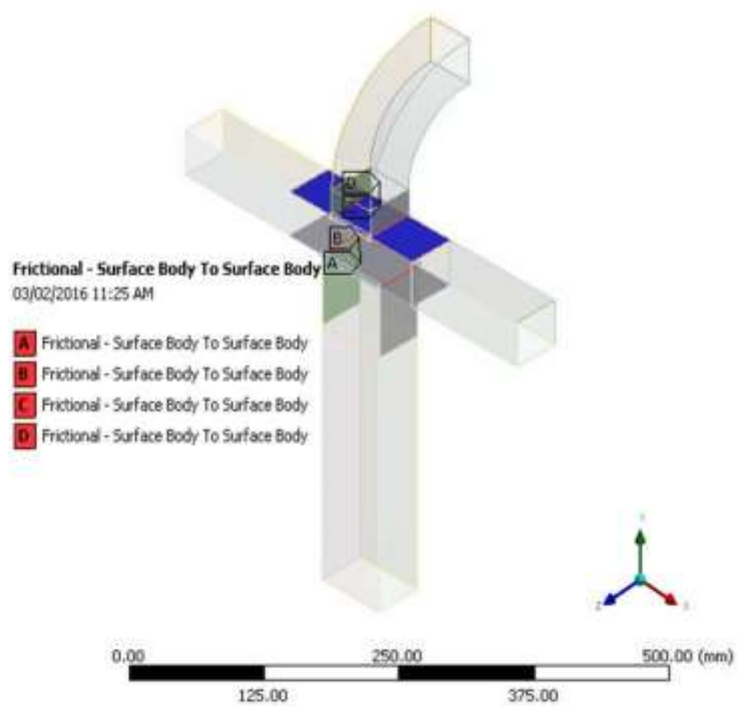

Figure 34: Frictional Contacts of Full Model

The contact regions of the submodels were defined using the basic concept of full model. In the submodels, the contact between the weld and the tube surface was defined as "bonded" type contact. The contact between the tubes surface was assigned as frictional contact. The frictional coefficient value 0.75 was used. The detail contact regions of the submodel are shown in Figure 35.

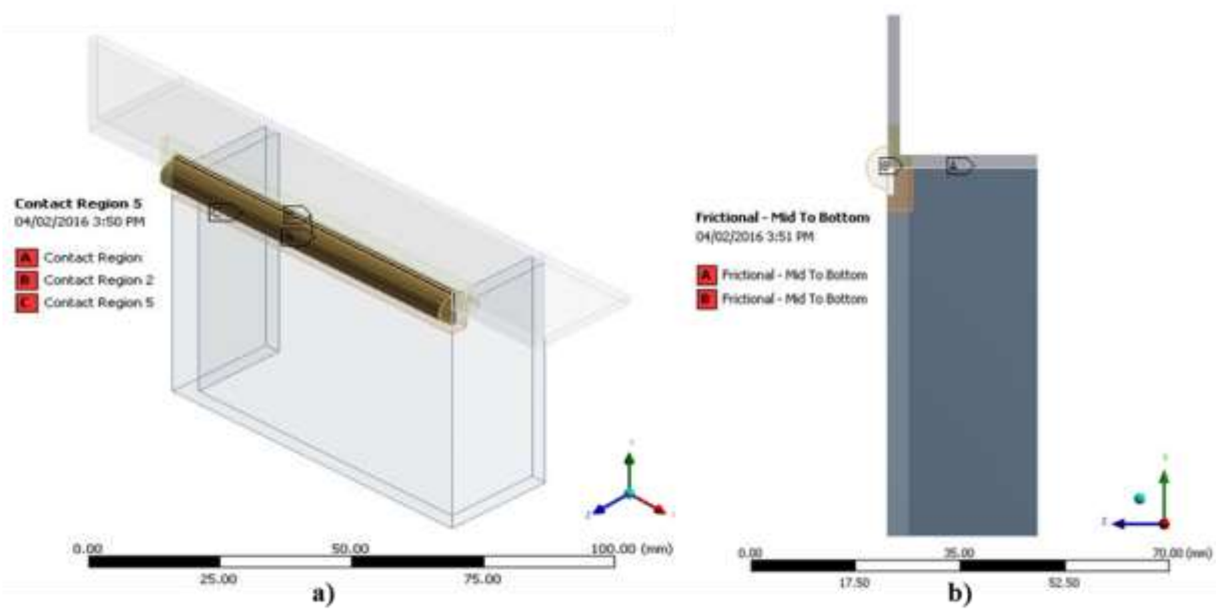

Figure 35: Contact Regions of the Submodel a) Bonded Contact b) Frictional Contact

3.3.2.4 Boundary Conditions

The experimental analysis on the window pillar was conducted under braking load conditions. To represent this real experimental condition, the following boundary conditions were applied to the full window pillar model.

a) The top end and the two side ends were fixed.

b) The force was applied at the lower end along the X-direction.

Figure 36 represents the applied boundary conditions of the full model.

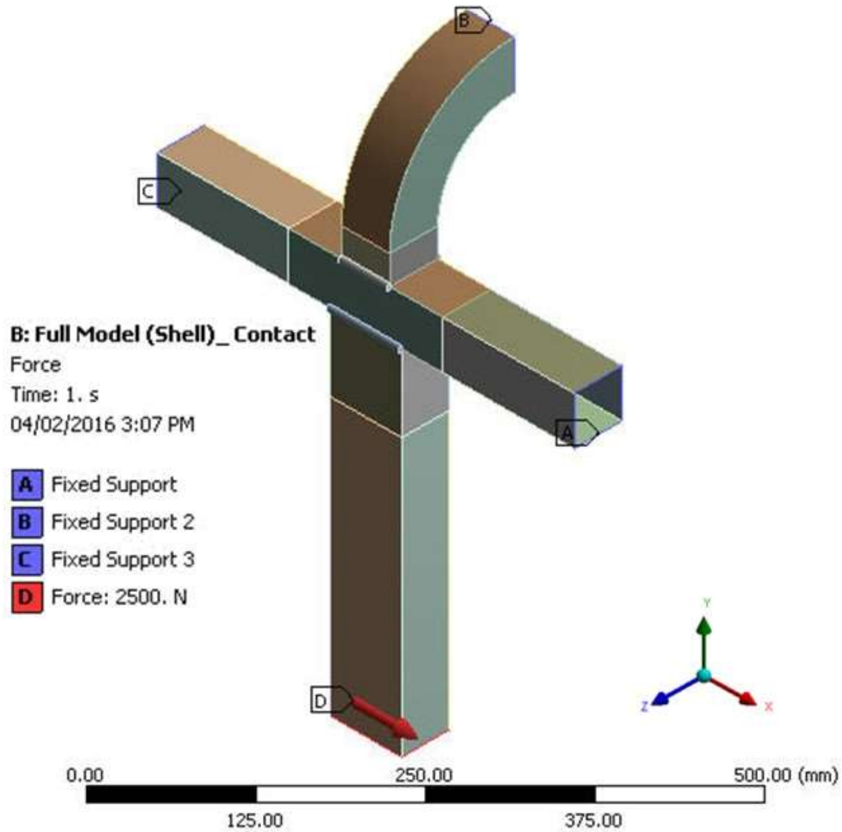

Figure 36: Boundary Conditions of the Full Model

3.3.2.5 Material Properties of Full Model

The initial full model was analyzed by assigning the mechanical properties of SS41003 for BM and AWS ER 308L for the weld from the literature review [43].

3.3.2.6 Initial Simulation

After assigning proper connection, boundary conditions and material property to the full meshed model, the model was ready for simulation. At first, simulation was conducted for 500 N Load and then the results were transferred to the submodel using the Shell to Solid transfer key. From the full model to submodel, cut boundary interpolation was performed by importing displacement.

3.3.2.7 Cut boundary Interpolation

To perform the cut boundary interpolation, the resulted displacements of the full model under loading condition were applied to the cut boundary of the submodel. The below Figure 37 shows cut boundary interpolation from the full model to submodel. The displacement of the appropriate bodies whose displacements were transferred at the cut boundary of the submodel was selected carefully. It ensured that the imported displacement of the submodel will represent the real condition of the full model simulation.

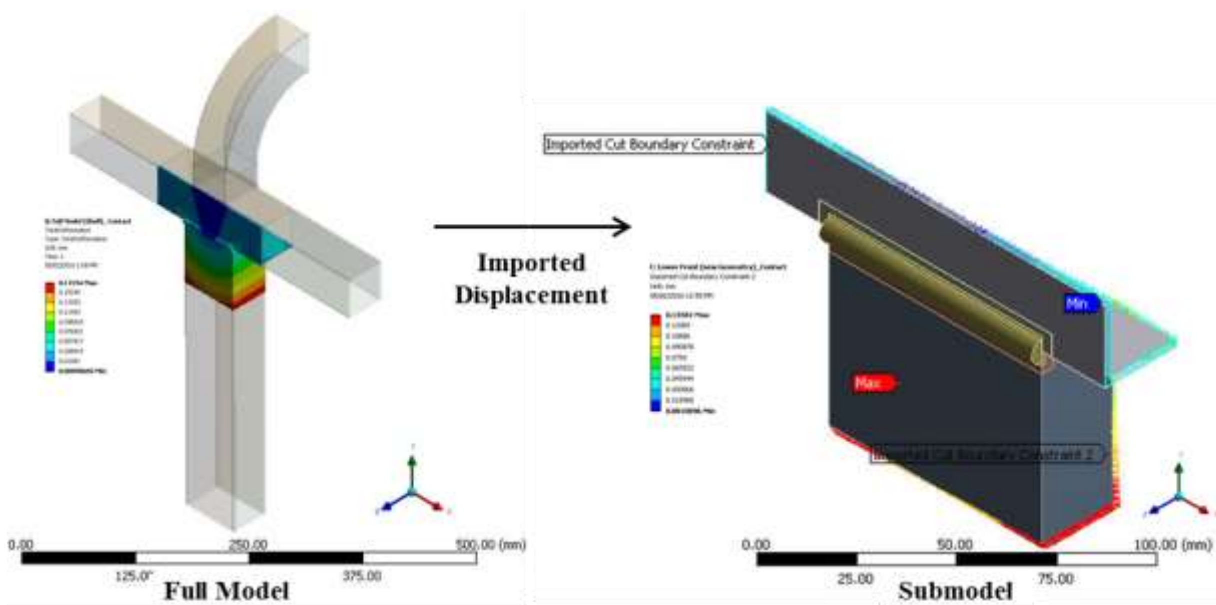

Figure 37: Cut Boundary Interpolation from Full Model to Submodel

3.3.2.8 Verification of Submodel

After importing displacement, the submodels are simulated. It is necessary to verify the result of the submodel for the reliability of the solution. To meet this purpose the results of the full and submodel were compared near the cut boundaries [47]. It should be noted that the both model were compared using the same material property.

Figure 38 shows the equivalent stress distribution of the full model and submodel. The full model and submodel exhibit same equivalent stress distribution pattern. Figure 39 represents the equivalent stress distribution of full model and sub model at one the cut boundary. The equivalent stress values at the cut boundary of the full model were also compared. Figure 39 and Table 1 ensure the validity of this submodel method.

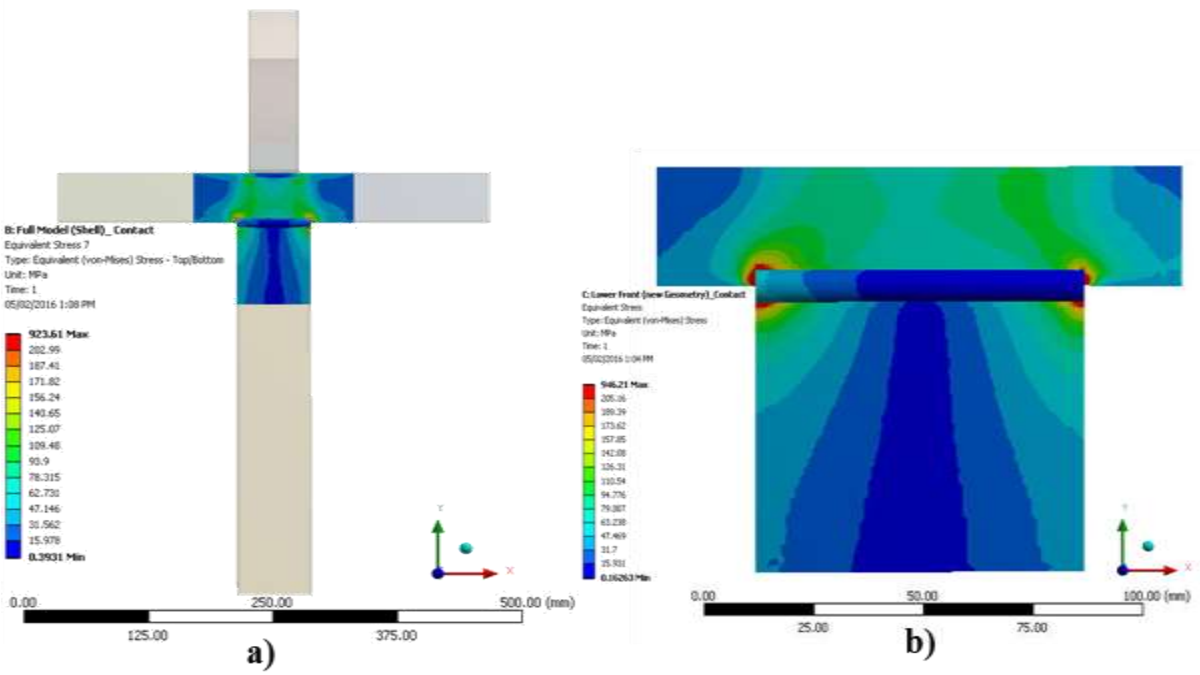

Figure 38: Equivalent Stress Distribution a) Full Model b) Submodel

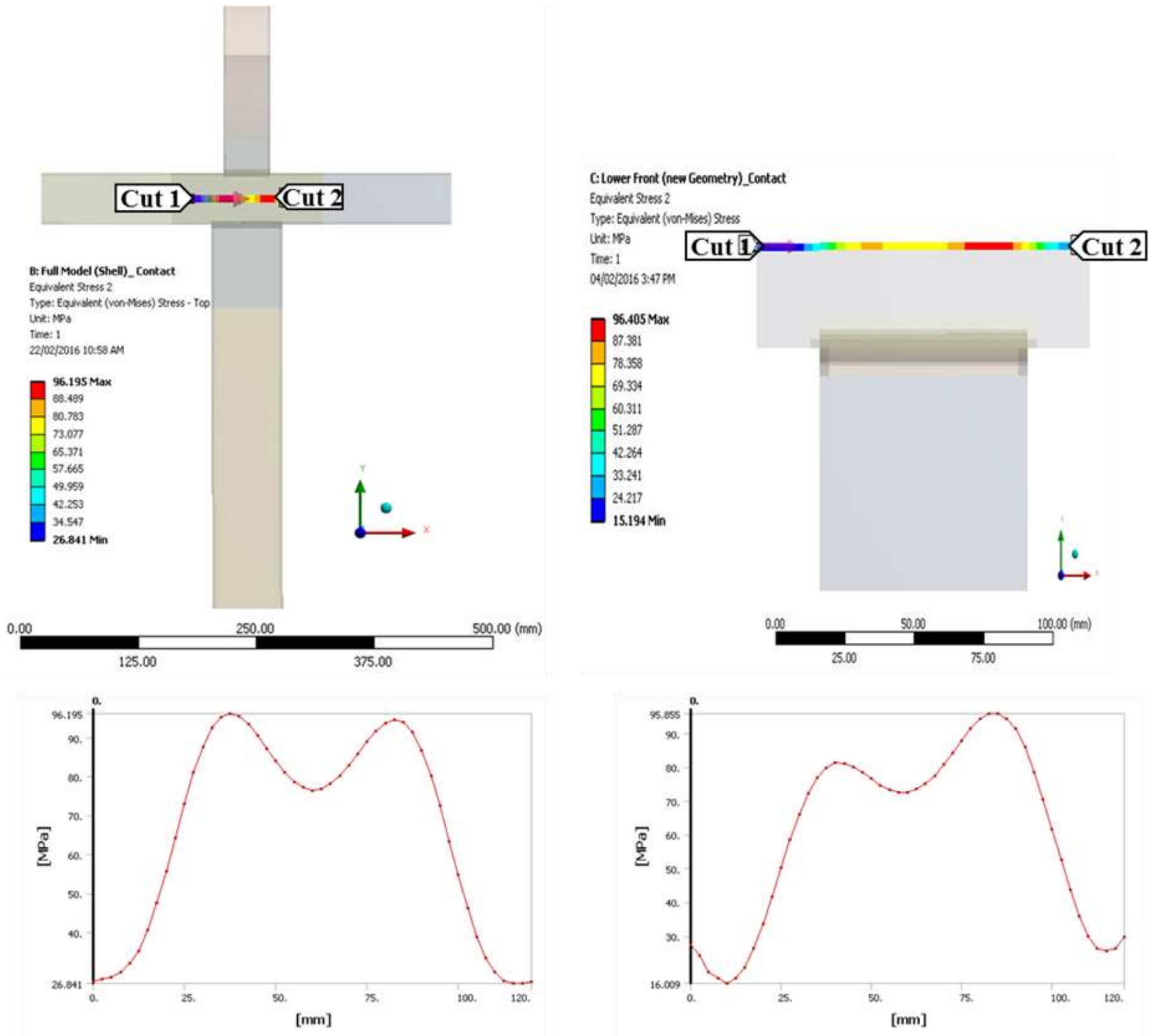

a) b)

Figure 39: Equivalent Stress Distribution at Cut Boundary a) Full Model b) Submodel

Table 1: Comparison of Equivalent Stress

Location	Full Model (Shell), MPa	Submodel (Solid), MPa
Cut 1	27.34	26.96
Cut 2	27.18	29.31

3.3.2.9 Material property of Submodel

In the next step, the submodel was analyzed using the experimentally gained material property. The experimental value of Young's modulus and Poisson ratio of HAZ obtained from the tensile testing of the ASTM standard specimen has been applied to the submodel. The Young's modulus of BM was used from the tensile testing of the BM sample of the window pillar joint. The Young's modulus of the FZ was used from the literature.

3.3.2.10 Final Simulation

The simulations of submodel were conducted at 500 N, 1000 N, 1500 N, 2000 N and 2500 N loading condition of full model to compare the result with experimental analysis.

CHAPTER 4

RESULTS AND DISCUSSION

The result analysis of this work is presented in this chapter. This section consists of two subsections. In section 4.1, the obtained HAZ width and mechanical properties of HAZ and BM zone of ASTM standard specimen have been presented along with the results obtained from braking load testing of window pillar structure. The mechanical properties of BM of window pillar have been presented here also. In section 4.2, the FEA results of ASTM standard specimen and window pillar structure have been discussed. A comparative analysis between the developed FEM model and another FEM model based on the effective notch for predicting stress behavior around the weld of the same window pillar structure has also been presented here.

4.1 Experimental Results

This subsection consists of two parts. In the first two-part experimental result of ASTM standard specimens have been presented. The following two parts present the result of experimental analysis on the window pillar structure.

4.1.1 Determination of Heat Affected Zone Width of ASTM standard Specimen

The prepared metallographic sample was examined under the optical microscope (Figure 15). The prepared specimen was placed on the stage of the microscope in such a way that its surface is perpendicular to the optical axis. This microscope has a system of lenses (W-Pl 10X/23) with which magnification up to 10X can be achieved.

Under the optical microscope, there is a clear microstructural difference between HAZ, BM zone and FZ. The observed microstructural difference is presented in Figure 40.

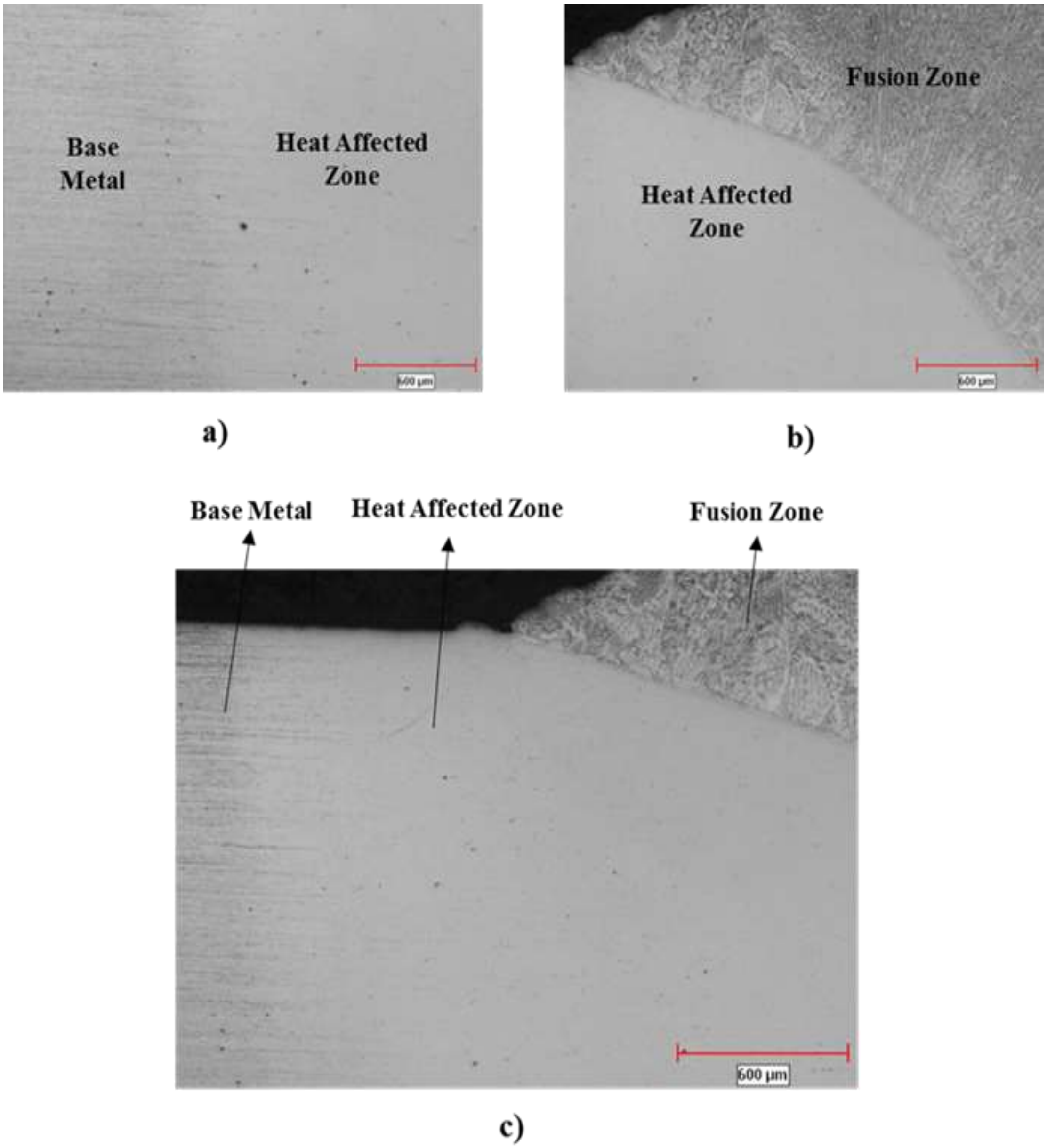

Figure 40: Microstructural Difference between Base Metal, Heat Affected zone and Fusion Zone

From this microstructural change the HAZ width from the fusion line has been calculated. The microstructural change suggests the HAZ width of 1.1 mm at the top of the sample from the fusion line whereas at bottom the HAZ width becomes around 4.25 mm (Figure 41).

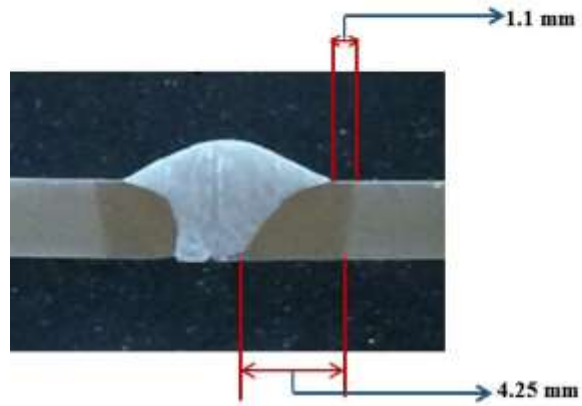

Figure 41: Heat Affected Zone Width

4.1.2 Determination of Material Properties of Heat Affected Zone (HAZ) and Base Metal (BM) Zone of ASTM Standard Specimen

The tensile testing of the ASTM standard was performed at different loading points (250 N, 500 N, 750 N, 1000 N, 1250 N, and 1500 N). The obtained data from two strain gauges (3D rosette) were converted into normal strain and shear strain component using Equation (3) -(5). The experimental results indicate one dominant normal strain along the loading direction. Figure 42 shows normal strain distribution at strain gauge 1 position which is located at HAZ region.

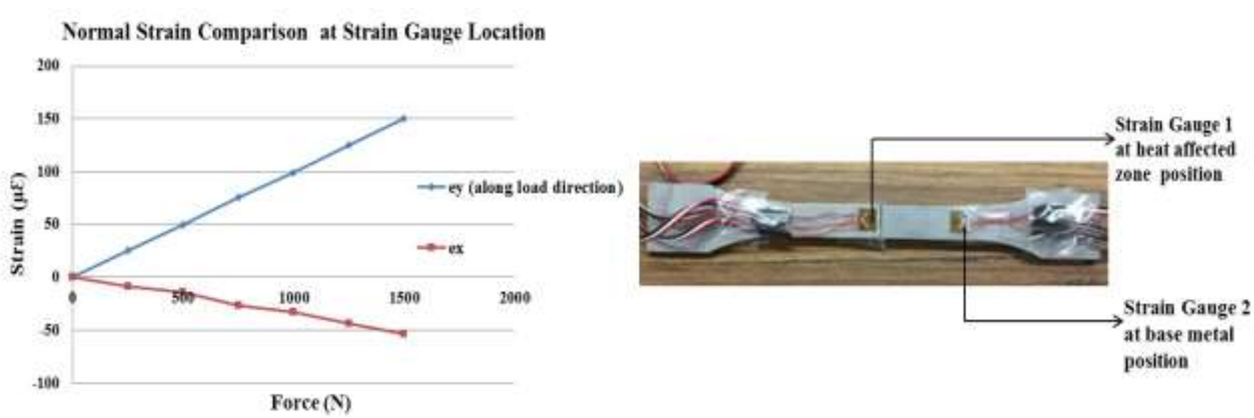

Figure 42: Normal Strain Distribution at Strain Gauge 1 Position

The graph represents that the normal strain along loading direction is significant. Normal strain in another direction is quite negligible. Shear strain is also very negligible compared to normal strains result.

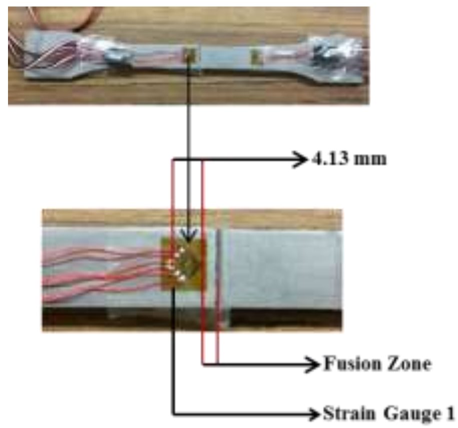

Figure 43: Strain Gauge 1 Attached at Heat Affected Zone

The gauge length of attached strain gauge 1 at the HAZ is around 4.13 mm (Figure 43). This gauge covers the full HAZ area at the bottom of the specimen.

The HAZ area is not homogenous, so this strain gauge determines the average strain over the gauge length region. Therefore, the obtained Young's modulus from the slope of the stress vs. strain (along loading direction) curves of the HAZ represents an average Young's modulus of the HAZ region. On the other hand, the strain gauge in BM zone shows Young's modulus of that region. The stress vs. strain curve of the HAZ and BM zone are shown in Figure 44. The tensile testing was conducted under different loading conditions within the elastic limit. So, these two stress vs. strain curves show the behavior of the HAZ region and BM zone within the elastic range.

The slope stress vs. strain curve of the HAZ suggests that the average Young's modulus across the HAZ is 278.2 GPa while Young's modulus of the BM zone is found to be 211.9 GPa.

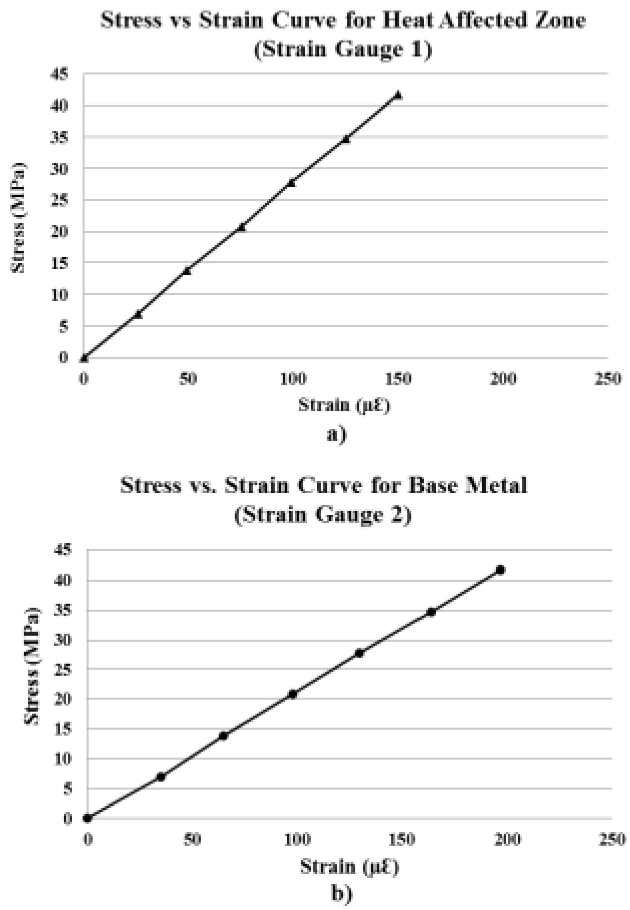

Figure 44: Stress vs. Strain Curve for a) Heat Affected Zone b) Base Metal Zone

Poisson's ratio is calculated from the ratio of the lateral strain to axial strain . Poisson's ratio of the HAZ is recorded 0.35 while for BM the Poisson's ratio is 0.31.

4.1.3 Braking Load Testing of Window Pillar Structure

The testing of window pillar structure under braking load condition was performed at different loading points (500 N, 1000 N, 1500 N, 2000 N and 2500 N). The obtained data from six strain gauges (3D rosette) were converted into normal strain and shear strain component using

Equation (3)-(5).

The experimental setup and results of the real structures are not presented here due to industrial confidentiality.

4.1.4 Determination of Material Properties of Base Metal of Window Pillar Structure

Tensile testing was performed on the two BM samples of the window pillar structure. One sample was collected from the middle tube and another one was collected from the lower tube. The samples were tested until it breaks. So, complete tensile profiles were obtained for both the samples.

Young's modulus of the lower and middle tube is obtained from the slope of the linear part of stress vs. strain curve. The Young's modulus of the lower tube is 193 GPa where for the middle tube the modulus is 203 GPa.

4.2 Finite Element Analysis (FEA) Result

In the first part of this subsection, FEA results of ASTM standard specimen have been discussed. The FEA results of window pillar structure are presented in the following part.

4.2.1 ASTM Standard Specimen

The experimentally obtained HAZ width 1.1 mm to 4.25 mm (from the top to bottom) and Young's Modulus and Poisson ratio of HAZ and BM zone have been applied to the finite element model of ASTM standard specimen (Figure 45). The Young's modulus of the FZ was used from the literature [43]. Therefore, the simulation of the FEM model is performed using the following properties:

Table 2: Mechanical Properties used in ASTM standard FE Model

Type	Young's Modulus, GPa	Poisson's ratio
Heat Affected zone	278	0.35
Base Metal	211	0.31
Fusion Zone	200	0.3

The results found from finite element modeling have been compared with the experimentally obtained tensile testing results. Figure 46 shows the normal strain distribution in the loading direction of the ASTM standard specimen.

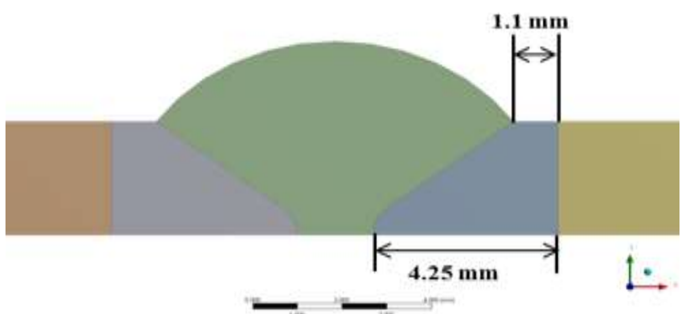

Figure 45: Heat Affected Zone width in Finite Element Model of ASTM Standard Specimen

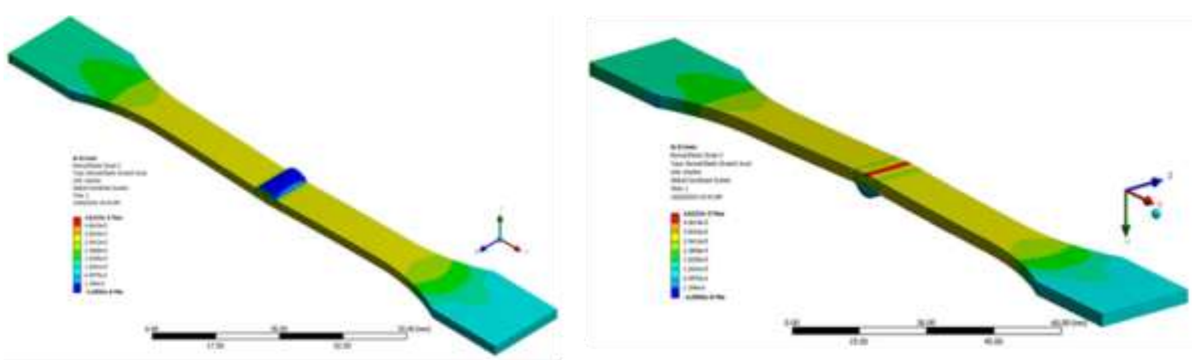

a) b)

Figure 46: Normal Strain Distribution in the Loading Direction of ASTM Standard Specimen in FEA a) Top b) Bottom

A good agreement has been found between the FEA results and experimental results as shown in Figure 47. Figure 47 represents the comparison of normal strain in the tensile loading direction between experimental and FEA result on strain gauge 1 location. There is only 4-8 % difference between the finite element model result and experimental result.

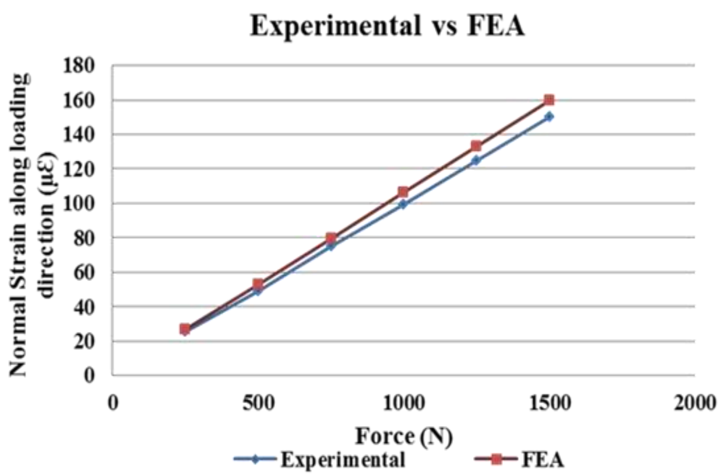

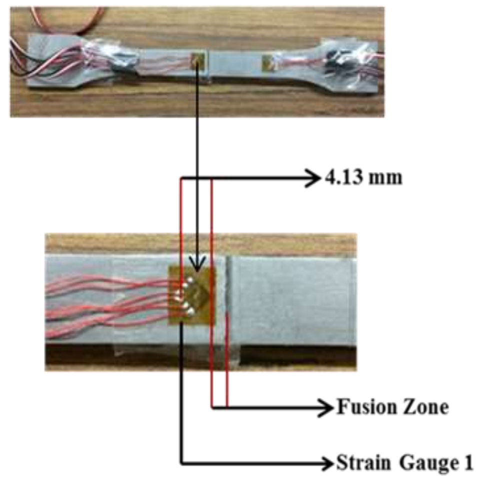

Figure 47: Comparison of Normal Strain Distribution between Experimental and FEA Result at Strain Gauge 1 Location

Table 3: Comparison of Experimental and FEA result at Strain Gauge 1 Location of ASTM standard Specimen

Load (N)	Experimental Strain (µƐ)	FEA Strain (µƐ)	Difference (%)
250	25.73	26.58	3.30
500	49.25	53.15	7.93
750	75.36	79.72	5.78
1000	99.17	106.30	7.19
1250	125.03	132.88	6.28
1500	150.11	159.45	6.22

4.2.2 Window Pillar Structure

After verification of the submodel, the simulations FEA of the submodel were conducted considering the welding phenomenon. In this regards, the experimentally obtained HAZ width, Young's modulus, Poisson ratio from the ASTM standard sample and Young's modulus of BM tube obtained from the tensile testing of the BM were applied to the submodel. In this case also Young's modulus of the FZ was used from the literature. Therefore, the FEA of the submodel is performed using the following properties:

Table 4: Mechanical Properties used in Window Pillar FEM Model

Type	Young's Modulus, GPa	Poisson's ratio
Heat Affected Zone	278	0.35
Base Metal (Middle Tube)	203	0.3
Base Metal (Lower Tube)	193	0.3
Fusion Zone	200	0.3
Heat Affected Zone Width: 1.1 mm		

The FEA results from the submodel have been compared with the experimentally obtained results under braking load. The experimental results under braking load exhibit larger shear strain in some locations. If normal or principle strain was used to compare the experimental and FEA result, then the effect of shear strain was neglected. So to accumulate all the strains result in one parameter, the equivalent stress is used to compare the two results. Moreover, equivalent stress is widely used by the designer's as design criterion. Equations (3) -(13) were used to convert all the normal and shear strain into equivalent stress.

The equivalent stress distribution of the front submodel is shown in Figure 48.a. The FEA result of equivalent stress at the three front side strain gauge locations were compared with the experimentally obtained equivalent stress. The locations of the strain gauges on the window pillar structure were measured using pixel ruler.

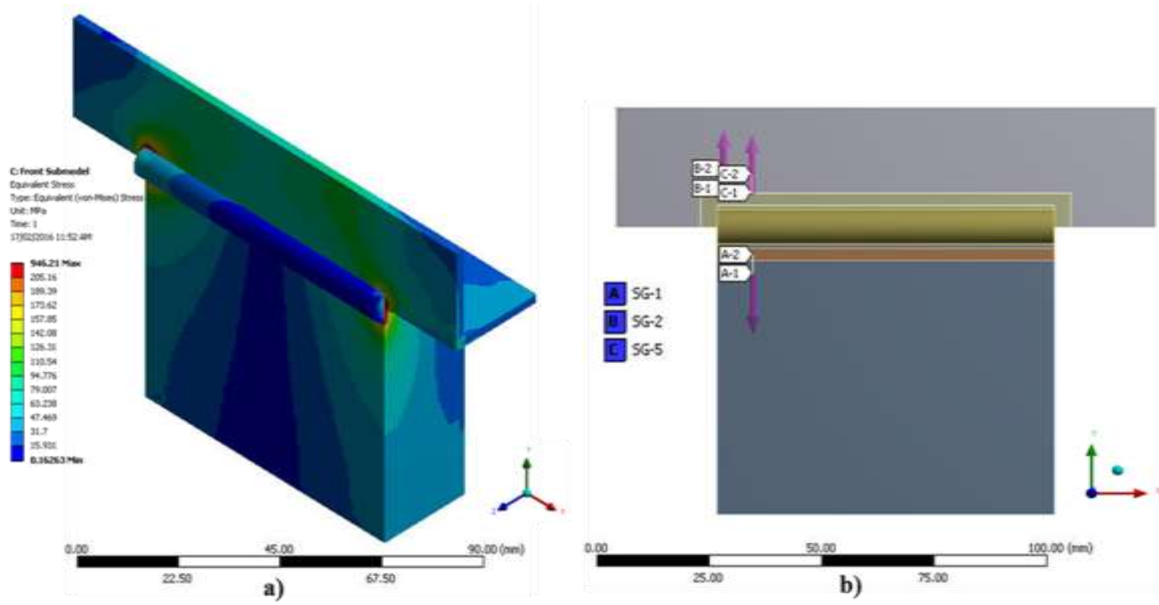

Figure 48: Front Submodel a) Equivalent Stress Distribution b) Strain Gauge Location

Table 5: Equivalent Stress Distribution at Strain Gauge 1, 2 & 5 Location of FEM Model Window Pillar Structure

LOAD (N)	**Equivalent Stress, σvm (MPa)**		
	Strain Gauge 1	**Strain Gauge 2**	**Strain Gauge 5**
500	15.77	23.73	24.77
1000	31.63	47.74	49.06
1500	47.54	71.81	73.53
2000	63.49	96.04	98.04
2500	79.48	120.48	122.60

It is observed from the comparison that the difference between experimental and FEA result for strain gauge 1 & 2 locations is around 12%-16%. But for strain gauge 5 location, the difference is about 24 %. So in the case of strain gauge 1 and 2 location, a good agreement between experimental and FEA is found but for strain gauge 5 location the difference is little higher.

Then the experimental and FEA results of the back side of the structure are compared. The equivalent stress distribution of the back submodel is shown in Figure 49.a.

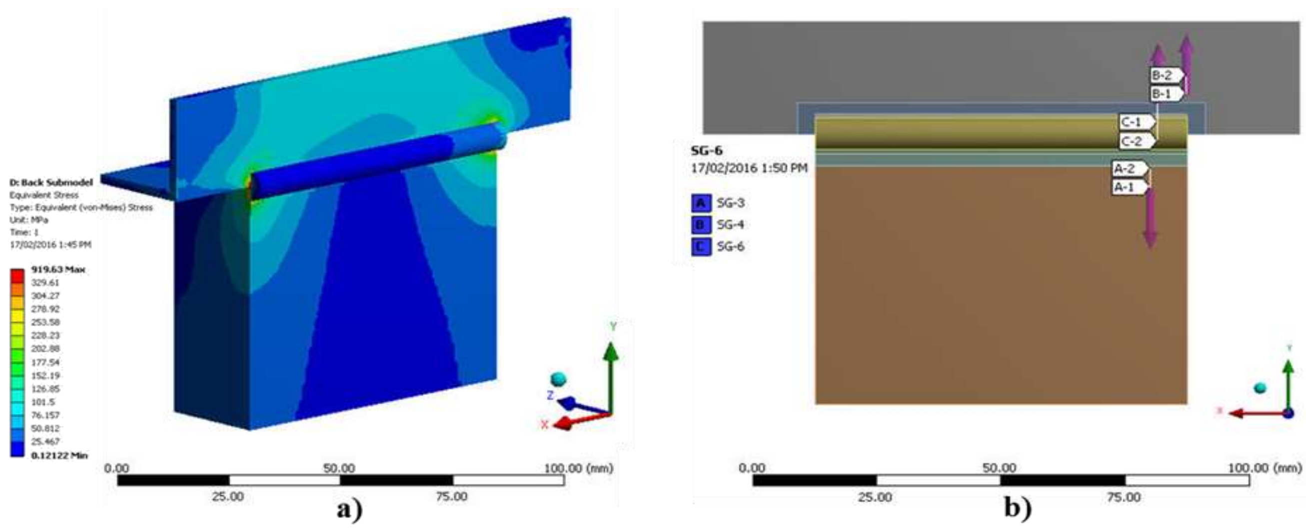

Figure 49: Back Submodel a) Equivalent Stress Distribution b) Strain Gauge Location

Table 6: Equivalent Stress Distribution at Strain Gauge 3,4 & 6 Location of FEM Model Window Pillar Structure

LOAD (N)	**Equivalent Stress, σvm (MPa)**		
	Strain Gauge 3	**Strain Gauge 4**	**Strain Gauge 6**
500	13.78	20.23	25.77
1000	27.65	40.62	51.46
1500	41.58	61.08	77.12
2000	55.54	81.60	102.76
2500	69.54	102.26	128.49

A similar trend in the result is found from the finite element analysis of the submodel of the back side of the structure like front side. In the back side, the difference between experimental and FEA result is about 17% to 18 % for strain gauge 3 & 4 locations. But for strain gauge 6 location, the difference is about 34 %. So like strain gauge 5, the deviation from the experimental result is also high at the strain gauge 6 location. Like strain gauge 1 & 2, the good agreement between experimental and FEA result is found at strain gauge 3 & 4 location.

The above finite element analysis result is found for HAZ width 1.1 mm which was obtained from the top surface of the ASTM standard specimen. But the HAZ width varies from 1.1 mm to 4.25 mm from the top to bottom surface of the ASTM standard specimen. So the developed FEM model is also simulated by increasing the HAZ width in Y and Z direction (Figure 50). The simulation is carried out on the submodel of the back side of the structure.

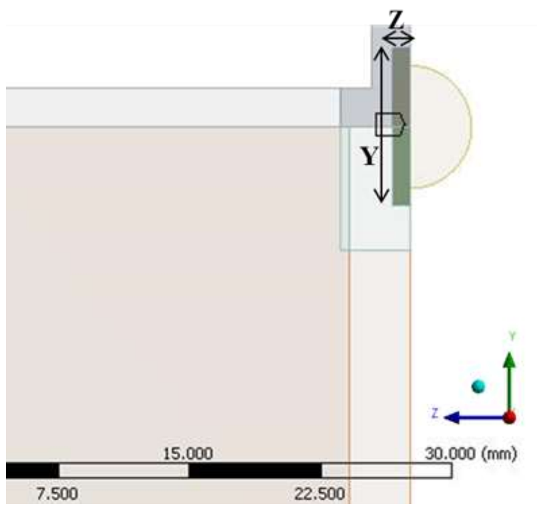

Figure 50: Direction of Heat Affected Zone Width Increase

From the simulation result, it is observed that when HAZ increased in both Y and Z direction then experimental and finite element analysis result difference decrease for strain gauge 3 and 4 location but increase for strain gauge 6 location. No significant effect is found for increased HAZ width in Y direction for any strain gauge. So from this investigation, it is evident that the best matches for all three strain gauges are found for HAZ width 1.1 mm.

An analysis is carried out to find out the higher deviation of strain gauge 5 & 6 location. It is an interesting thing to notice that both strain gauge 5 & 6 are located above the lower weld which are close to the mid position of the structure. In these locations, higher shear strain was found compared to other strain gauge position.

To model the window pillar for finite element analysis the small fillet radius of the original specimen was not considered. The window pillar model is simplified because with that small fillet radius the number of mesh elements becomes too high that cannot be solved with the existing system. Moreover, another important point is that the weld thickness was not uniform throughout the tube length. At the side weld thickness is higher than the middle portion of the tube (related picture is not given here due to confidential issue).

So at strain gauge 5 & 6 location geometry simplification effect i.e. fillet modification of lower and middle tube and welding thickness change both exists which might results in a large difference of FEA result from experimental result.

The experimental stress behavior was also compared with the FEA stress behavior to investigate whether this finite element model can predict the stress behavior of the structure. Figure 51 presents the FEA stress behavior of the window pillar structure.

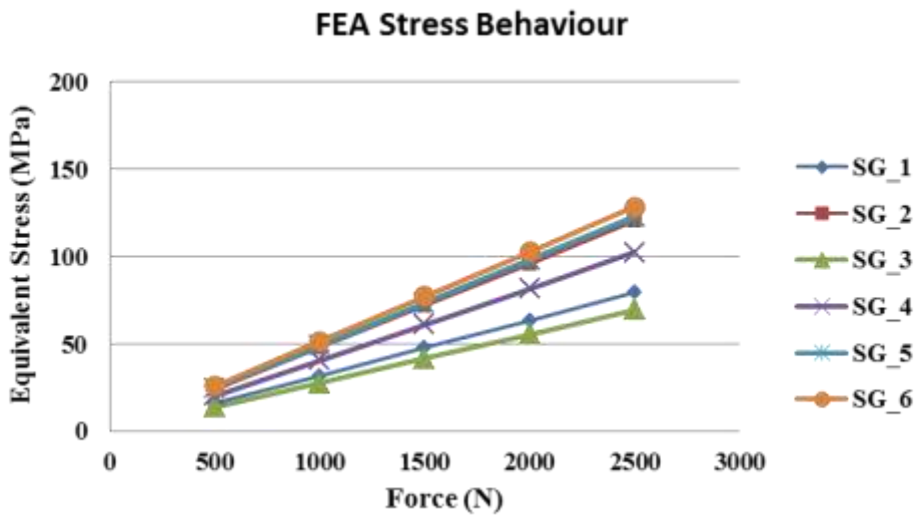

Figure 51: FEA Stress Behavior of the Window Pillar Structure

Figure 51 presents that the higher equivalent stress is found at strain gauge 6 location and lower equivalent stress is found at strain gauge 3 location. This similar pattern is also found in the experimental analysis. So from this comparison, it can be said that the developed FEM model can predict the stress behavior around the weld of the window pillar structure.

4.2.3 Comparison of Material Based Model and Effective Notch Model

The result from the above mentioned FEM model with material property is compared with the FEM model using the effective notch stress approach developed for the same window pillar to predict stress behavior of welded structure. The effective notch stress model is geometry sensitive to tune the equivalent size of the notches around the welding joints so as to match the stress distribution obtained from the experimental studies [48]. So, the FEM model based on effective notch stress approach can be termed as effective notch model and the above mentioned model can be termed as material based model.

As described in this thesis, the material based model is developed considering the material property change around the weld i.e. HAZ width and Young’s Modulus. For this model, the optimum FEA solution is found for experimentally obtained HAZ width 1.1 mm and HAZ Young’s Modulus 278 GPa. The material based model is mainly sensitive to welding process and welded structure material. In the material based modeling, shell to solid submodeling technique is used and results are extracted from solid submodel.

On the other hand, the effective notch model is developed by using the concept of effective notch stress approach. The effective notch radius depends on the structural geometry, weld type and weld size. For the window pillar the optimum value of the effective notch radius is found 0.5mm. In this technique, the material properties of the heat affected zone are assumed to be same as the base metal, which is the main difference from the material based model developed on this thesis. This modeling technique is limited to geometry variation. The effective notch model is developed using shell element (only welds are solid element)

The comparative study between the stress distributions around the window pillar welding joint from these two models are presented in Figure 53 and Figure 54.

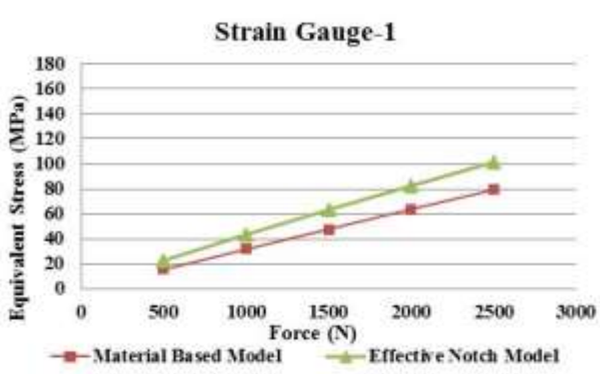

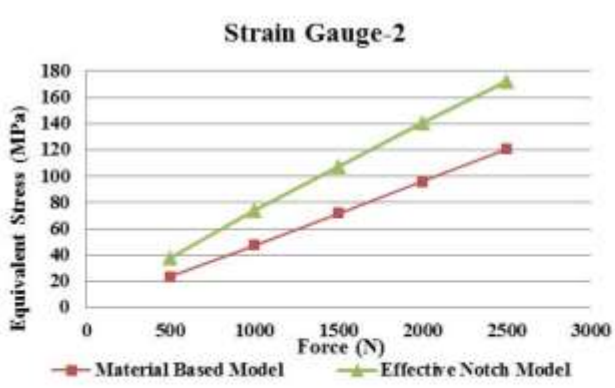

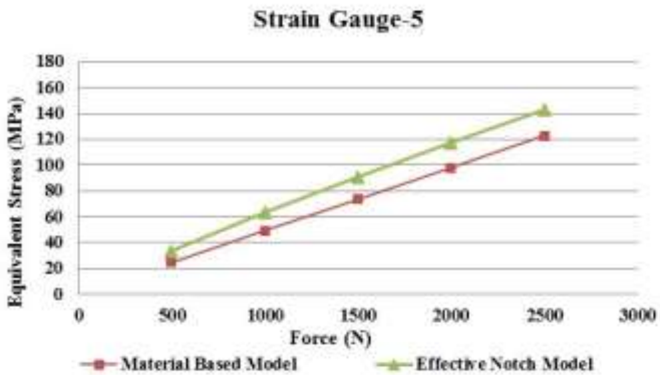

Figure 52: Comparison between Material Based Model and Effective Notch Model Stress at Strain Gauge 1, 2 & 5 Location

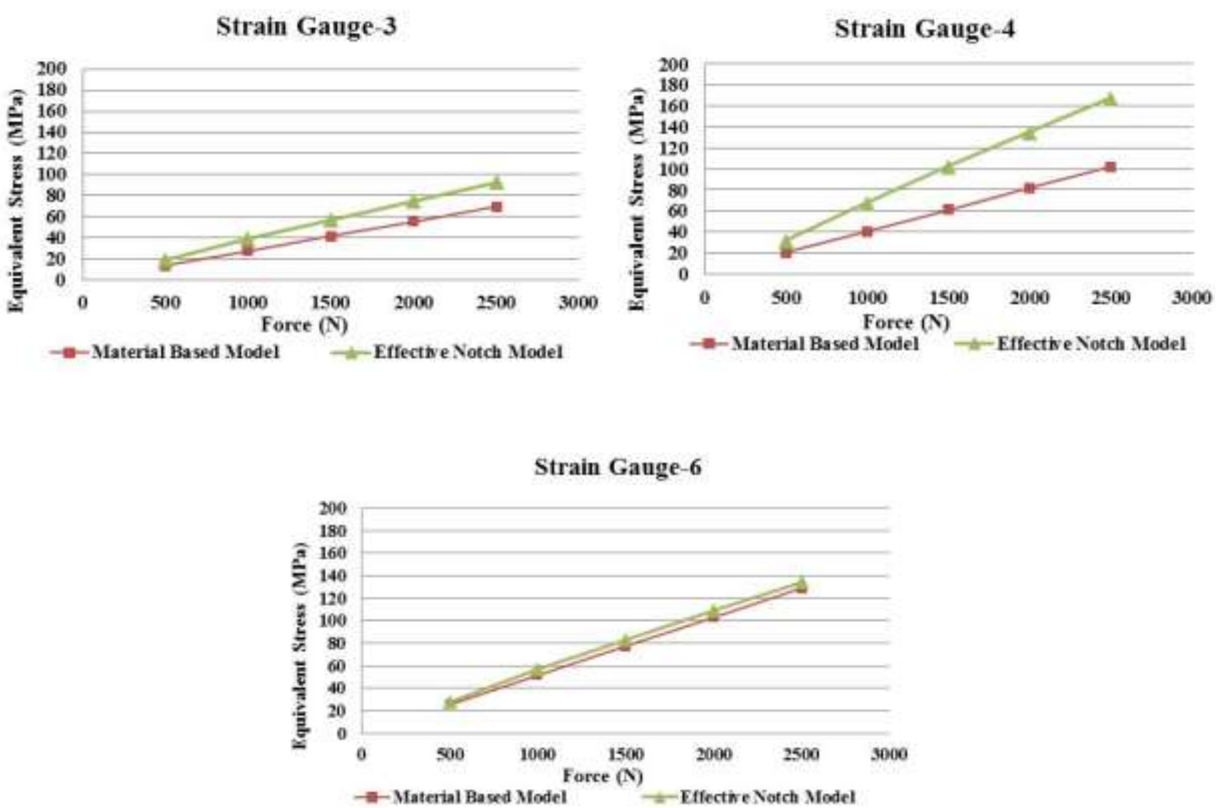

Figure 53: Comparison between Material Based Model and Effective Notch Model Stress at Strain Gauge 3, 4 & 6 Location

The above comparison suggests that in the material based model, the developed equivalent stress is always lower than the developed equivalent stress in the effective notch model. Moreover, when these two models are compared with the experimental result, it is observed that the experimental equivalent stress value lies in between these two model at strain gauge 1, 2, 3 & 4 location whereas at strain gauge 5 & 6 the experimental result is higher than the both model. (The experimental results of the real structures are not presented here due to industrial confidentiality). It suggests that, the material based model always exhibits lower equivalent stress than the experimental stress value whereas in the effective notch model the developed equivalent stress is sometimes higher and sometimes lower than the experimental stress value.

From the stress behavior of the material based model (Figure 51), it is observed that the highest equivalent stress is developed at strain gauge 6 location and lowest equivalent stress location is strain gauge 3. The experimental equivalent stress behavior also exhibits same pattern. But in the effective notch model, the highest equivalent stress location is strain gauge 2.

The above discussion states that the material based model based on the experimentally obtained HAZ width 1.1 mm and HAZ Young’s Modulus 278 GPa can be very useful for prediction of stress behavior around the weld for any arc welded joint of stainless steel irrespective of its geometry. But the model is sensitive to the welding process and material change. The advantage of this model is that it’s under predicting the stress at all locations from the experimental stress, so this model can be used with a reasonable average design factor.

On the other hand, in the effective notch model material property change is not considered and this model based on the tuning of notch radius (optimum notch radius is 0.5 mm for this structure). This effective notch model is sensitive to geometry. This model can be useful for any material as its not material sensitive but for different geometry and different type of welding process the model is not applicable. Moreover, as this model gives lower stress at some location and higher stress at other location than experimental result at a same time so the error bar will significantly increase and it will be difficult to set a design factor.

CHAPTER 5

CONCLUSIONS AND FUTURE WORK

The mechanical properties of welded joint changes significantly around the HAZ. So the properties of HAZ have great influence on the behavior of a welded structure. The main focus of this research is to develop a FEM model of an arc welded stainless steel structure which can predict the stress behavior of a welded structure. To comply with this objective, the changes of mechanical properties of welded joint were considered and experimentally tested to develop the FEM model.

The experimental analysis was performed to find out the width of HAZ of an ASTM standard arc welded stainless steel specimen by observing the microstructural change using the optical microscope. The microstructure shows significant variation throughout the HAZ, BM zone and FZ. An increase in the HAZ width is observed along the thickness direction of the samples. The Young's modulus and Poisson ratio of the HAZ and BM zone were derived from the tensile testing of ASTM standard specimen. The experimental analysis result implies a considerable higher value of Young's Modulus in the HAZ compared to the BM zone.

An experimental analysis was also performed on a real arc welded stainless steel frame structure to find out the strain behavior around the HAZ. The tensile testing of the sample of the real structure was also performed to find out the Young's modulus value of BM.

The experimentally obtained HAZ width, Young's modulus of HAZ and respective BM zone were then applied to the finite element models of an ASTM standard arc welded joint as well as a real arc welded structure of the same material. The finite element analysis results in both cases are in good agreement with the experimental results. So, the developed material property based FEM model can predict the stress behavior around the weld.

In this thesis, submodeling approach is used for finite element analysis of the real frame structure. This approach can be very useful for analysis of a small or critical part of a large engineering or vehicle structure in details. This shell to solid submodeling technique is also proved to be convenient to explain stress intensity accurately. But required attention is necessary to guarantee the reasonable result. In this regard, the verification of the submodels results is also presented in this research.

The most challenging part of this work is to implement this shell to solid submodeling technique. Previously, solid to solid submodeling technique was used by different researcher. But, this shell to solid submodeling is a new concept introduce in ANSYS 15 workbench. This new concept is successfully used in this research for modelling of welded joint with reasonable results and much more efficient calculation process. There are some important points which should be considered before using this developed finite element modeling technique. The main significance of this developed FEM model is, it is applicable for any arc welded joint of stainless steel irrespective of its geometry. That's why FEA results in both case (ASTM standard specimen and window pillar) shows good agreement with experimental result for HAZ width 1.1 mm and HAZ Young's modulus 278 GPa. But, this research is mainly focused on the geometry of the frame structures of heavy ground vehicles. Another important point is, the HAZ width and mechanical properties can be different for different welding processes and different materials. So, for different type of material and welding process it's recommended to do the experimental studies. Moreover, as the properties of HAZ is not homogenous, the Young's modulus of the HAZ obtained from the tensile testing using the strain gauge only gives an estimation of average Young's modulus value throughout the HAZ region.

The following recommendation can be made as future work,

I. In this research, the average Young's modulus of the HAZ is evaluated. New techniques such as UltraMARS (Ultrasonic Measurements of Applied and Residual Stress) can be studied to find out the mechanical properties i.e. Young Modulus and Poisson ratio at different points of HAZ of arc welded joint of stainless steel leading to better understanding of the materials properties of the HAZ and its more accurate modeling process. This can help to increase the accuracy of the model.

II. The mechanical properties of FZ were not determined as it was not possible to attach strain gauge on the rough curved surface of the weld. Therefore, new methods/sensors can be explored/ developed to find out the FZ properties. It will also help to increase the model accuracy.

III. Same experimental analysis procedure and FEM modeling techniques can be applied to the different types of welds of different materials. It will help to understand the mechanical behavior of different welding types and materials. It will be also useful to compare the validity of different FEM welding models.

REFERENCES

[1] "Wikipedia," October 2015. [Online]. Available: https://en.wikipedia.org/wiki/Structural_integrity_and_failure. [Accessed January 2016].

[2] "Wikipedia," December 2015. [Online]. Available: https://en.wikipedia.org/wiki/Welding. [Accessed January 2016].

[3] M. Koçak, "Structural Integrity of Welded Structures: Process - Property – Performance (3P) Relationship," in *63rd Annual Assembly & International Conference of the International Institute of Welding,* Istanbul,Turkey, 2010.

[4] "EngineersHandbook," 2006. [Online]. Available: http://www.engineershandbook.com/MfgMethods/fastening&joining.htm. [Accessed January 2016].

[5] "Wikipedia," December 2015. [Online]. Available: https://en.wikipedia.org/wiki/Welding. [Accessed January 2016].

[6] S. David, S. Babu and J. Vitek, "Welding: Solidification and Microstructure," *The Journal of The Minerals, Metals & Materials Society (TMS),* vol. 55, no. 6, pp. 14-20, 2003.

[7] "Gas Metal Arc Welding: Product and Procedure Selection," THE LINCOLN ELECTRIC COMPANY, Cleveland, 2014.

[8] "Wikipedia," May 2015. [Online]. Available: https://en.wikipedia.org/w/index.php?title=Heat-affected_zone&action=history. [Accessed

January 2016].

[9] P. Mayr, Evolution of microstructure and mechanical properties of the heat affected zone in B-containing 9% chromium steels, Graz, 2007.

[10] A. Joarder, S. Saha and A. Ghose, "Study of Submerged Arc Weld Metal and Heat-Affected Zone Microstructures of a Plain Carbon Steel," American Welding Society, 1991.

[11] S. Missori and A. Sili, "Mechanical behaviour of 6082-t6 aluminium alloy welds," Teksid Aluminum, 2000.

[12] M. Beghini, L. Bertini and F. Puccio, "Evaluation of Mechanical Properties of Welded Joints by Small-Specimen Tests," *strain,* vol. 37, pp. 155-158, 2001.

[13] P. Yayla, E. Kaluc and K. Ural, "Effects of welding processes on the mechanical properties of HY 80 steel weldments," *Materials & Design,* vol. 28, no. 6, p. 1898–1906, 2006.

[14] M.-L. Zhu and F.-Z. Xuan, "Correlation between microstructure, hardness and strength in HAZ of dissimilar welds of rotor steels," *Materials Science and Engineering: A,* vol. 527, no. 16-17, pp. 4035-4042, 2010.

[15] M. P. Reddy, A. A. S. William, M. Prashanth, S. S. Kumar, K. D. Ramkumar, N. Arivazhagan and S. Narayanan, "Assessment of Mechanical Properties of AISI 4140 and AISI 316 Dissimilar Weldments," *Procedia Engineering,* vol. 75, p. 29–33, 2014.

[16] J. Y. Lee, J.-h. Moon, H. Kim and Y. H. Kim, "Evaluation of metal weld-zone by using Poisson’s ratio distribution," in *International Workshop of NDT Experts,*, Prague, 2011.

[17] A. S. Humaun Kabir, X. Cao, J. G. Baradari, P. Wanjara, A. Birur and M. Medraj, "Determination of Global and Local Tensile Behaviours of Laser Welded Ti-6Al-4V Alloy," *Advanced Materials Research,* vol. 409, pp. 859-864, 2011.

[18] K. Saranatha, A. Sharmab and M. Ramji, "Zone wise local characterization of welds using digital image correlation technique," *Optics and Lasers in Engineering,* vol. 63, pp. 30-42, 2014.

[19] S. Akbarnejad, Investigation on static strength of welded joints, Sweden, 2012.

[20] A. Blomqvist, "Mismatch in high strength steel weldment, Application ,research and development," SSAB, Oxelösund, 1995.

[21] Welding Handbook, SSAB, 2009.

[22] G. W. Krutz and L. J. Segerlind, "Finite Element Analysis of Welded Structures," American Welding Society, 1978.

[23] J. Fang, C. Hoff, B. Holman, F. Mueller and D. Wallerstein, "Weld Modeling with MSC.Nastran," MSC.Software Corporation,, Los Angeles, 1999.

[24] A. Al-Samhan and S. Darwish, "Finite element modeling of weld-bonded joints," *Journal of Materials Processing Technology,* vol. 142, no. 3, p. 587–598, 2003.

[25] Amada Miyachi America, [Online]. Available: http://www.amadamiyachi.com/glossary/glossweldnugget. [Accessed January 2016].

[26] N. C. Chee and A. R. A. Bakar, "Finite Element Modeling of Arc Welded Joints," *Jurnal*

Mekanikal, vol. 23, pp. 15-30, 2007.

[27] A. Anca, A. Cardona and V. Fachinotti, "Finite Element Modeling of Welded Joints," in *Asociación Argentina de Mecánica Computacional*, San Luis, 2008.

[28] T. Martin and G. Nicoletto, "Fatigue design of welded joints using the finite element method and the 2007 ASME Div. 2 Master curve," *Frattura ed Integrità Strutturale,* vol. 9, pp. 76 - 84, 2009.

[29] "Wikibook," May 2010. [Online]. Available: https://en.wikibooks.org/wiki/Advanced_Structural_Analysis/Part_I_-_Theory/Failure_Modes/Fatigue/Special_Members/Welded_Joints. [Accessed January 2016].

[30] M. Malikoutsakis and G. Savaidis, "An Approach To The Effective Notch Stress Concept To Complex Geometry Welds Focusing On The Fe Modeling Of Weld Ends," in *3rd ANSA & μETA International Conference*, Halkidiki, 2009.

[31] H.-B. Sim, "Effective Notch Stress Method for Fatigue Evaluation of Welded Joints in a Steel Bridge Deck," *International Journal of Railway*, vol. 5, no. 2, pp. 89-92, 2012.

[32] Ø. S. Fagnastøl, Approaches for assessment of weld fatigue and verification of the effective notch stress approach, Trondheim,, 2014.

[33] T. K. Kang, S. J. Kim, H. M. Kim and T. S. Choi, "Load Estimation Methods on Welded Joints Using Finite Element Analysis," in *Transactions of the Korean Nuclear Society Autumn Meeting*, Gyeongju, 2011.

[34] R. N. Mhetre and S. G. Jadhav, "Finite Element Analysis of Welded Joint," *International*

Journal of Instrumentation,, vol. 1, no. 3,4, pp. 116-120, 2012.

[35] R. K. Kassab, H. Champliaud, N. V. Le, J. Lanteigne and M. Thomas, "Experimental and Finite Element Analysis of a T-Joint Welding," *Journal of Mechanics Engineering and Automation,* vol. 2, pp. 411-421, 2012.

[36] C. Wei, J. Zhang, S. Yang and W. Tao, "Experiment-based regional characterization of HAZ mechanical properties for laser welding," *The International Journal of Advanced Manufacturing Technology,* vol. 78, no. 9, pp. 1629-1640, 2015.

[37] S. David, S. Babu and J. Vitek, "Application of Optical and Other Advanced Characterization Techniques to Understand Weld Microstructures," Oak Ridge National Laboratory, Oak Ridge, 2001.

[38] M. Louthan, "Optical Metallography," *Materials Characterizations, ASM International,* vol. 10, pp. 299-308, 1986.

[39] "Cornell Center for Materials Research - Education," Materials of Engineering, LSU, [Online]. Available: http://www.ccmr.cornell.edu/wp-content/uploads/sites/2/2015/11/Polishing-Guidelines.pdf. [Accessed January 2016].

[40] "Introduction to Tensile Testing," in *Tensile Testing Second Edition* , ASM International, 2004, pp. 1-12.

[41] "INSTRON," INSTRON, [Online]. Available: http://www.instron.us/our-company/library/test-types/tensile-test. [Accessed January 2016].

[42] "efunda," [Online]. Available:

http://www.efunda.com/formulae/solid_mechanics/mat_mechanics/strain_gage_rosette.cfm. [Accessed 2016 January].

[43] "China Steel Supplier," [Online]. Available: http://www.steelgr.com/Steel-Grades/Mould-Steel/aws-er308l.html.. [Accessed February 2016].

[44] R. Silva, "Submodeling in ANSYS WorkBench 14.5," in *ESSS Conference and ANSYS Users Meeting*, Atibaia, 2013.

[45] "Introduction to Contact," ANSYS, Inc. Proprietary, 2010.

[46] P. Cunningham, "CAE Associates," 2014 February. [Online]. Available: https://caeai.com/blog/why-use-mpc-based-contact-bonded-connections. [Accessed February 2016].

[47] T.-W. Kima, G.-M. Leea, W.-S. Choi, k.-H. Jeong, K.-K. Kim and J.-I. Kima, "Application of Submodel Method for the Structural Analysis of Integral Reactor Internals," in *Transactions of the Korean Nuclear Society Autumn Meeting*, Busan, Korea, 2005.

[48] M. Nuruzzaman, "Finite Element Modeling Of Welded Joints Using Effective Notch Stress Approach," 2016.

APPENDIX A- STRAIN DATA OF ASTM STANDARD SPECIMEN

Table 7: Normal and Shear Strain Data at Strain Gauge 1 (Heat Affected Zone) Location

Load (N)	**Normal Strain in X-direction, Ɛx (μƐ)**	**Normal Strain in Y-direction(Loading), Ɛx (μƐ)**	**Shear Strain, γ_{xy}**	**Poisson Ratio**
0	0.00	0.00	0.00	0.000
250	-8.96	25.73	0.71	0.348
500	-14.08	49.25	4.42	0.286
750	-26.82	75.36	2.74	0.356
1000	-32.93	99.17	9.36	0.332
1250	-43.85	125.03	7.79	0.351
1500	-53.58	150.11	18.11	0.357

Table 8: Normal and Shear Strain Data at Strain Gauge 2 (Base Metal) Location

Load (N)	**Normal Strain in X-direction, Ɛx (μƐ)**	**Normal Strain in Y-direction(Loading), Ɛx (μƐ)**	**Shear Strain, γ_{xy}**	**Poisson Ratio**
0	0.00	0.00	0.00	0.000
250	-11.00	35.00	0.93	0.314
500	-20.00	65.00	5.80	0.308
750	-30.00	98.00	8.31	0.306
1000	-39.00	130.00	12.29	0.300
1250	-48.00	164.00	19.27	0.293
1500	-62.00	197.00	23.79	0.315